



1 **Anthropogenic and natural controls on atmospheric $\delta^{13}\text{C}$ -CO₂**
2 **variations in the Yangtze River Delta: Insights from a carbon**
3 **isotope modeling framework**

4

5 Cheng Hu^{1,2*}, Jiaping Xu³, Cheng Liu⁴, Yan Chen³, Dong Yang⁵, Wenjing Huang², Lichen
6 Deng⁶, Shoudong Liu², Timothy J. Griffis^{7**}, and Xuhui Lee⁸

7 ¹ College of Biology and the Environment, Joint Center for sustainable Forestry in Southern China,
8 Nanjing Forestry University, Nanjing, 210037, China

9 ² Yale-NUIST Center on Atmospheric Environment, International Joint Laboratory on Climate and
10 Environment Change (ILCEC), Nanjing University of Information, Science & Technology, Nanjing,
11 210044, China

12 ³ Jiangsu Climate Center, China Meteorological Administration, Jiangsu Nanjing 210009, China

13 ⁴ Jiangxi Province Key Laboratory of the Causes and Control of Atmospheric Pollution, East China
14 University of Technology, Nanchang 330013, China

15 ⁵ Ningbo Meteorological Observatory, Ningbo 315012, China

16 ⁶ Ecological Meteorology Center, Jiangxi Meteorological Bureau, Nanchang 330096, China

17 ⁷ Department of Soil, Water, and Climate, University of Minnesota-Twin Cities, St. Paul, Minnesota,
18 USA

19 ⁸ School of Forestry and Environmental Studies, Yale University, New Haven, Connecticut, USA

20

21 Correspondence:

22 *Cheng Hu, College of Biology and the Environment, Joint Center for sustainable Forestry in Southern
23 China, Nanjing Forestry University, Nanjing, 210037, China. nihaohucheng@163.com or
24 huxxx991@umn.edu

25 ** Timothy J. Griffis, Department of Soil, Water, and Climate, University of Minnesota, St. Paul, MN
26 55108, timgriffis@umn.edu

27

28

29

30

31

32

33

34

35

36



37 **Abstract:**

38 The atmospheric CO₂ mixing ratio and its $\delta^{13}\text{C-CO}_2$ composition contain important CO₂ sink and source
39 information spanning from ecosystem to global scales. The observation and simulation for both CO₂ and
40 its carbon isotope ratio ($\delta^{13}\text{C-CO}_2$) can be used to constrain regional emissions and better understand the
41 anthropogenic and natural mechanisms that control $\delta^{13}\text{C-CO}_2$ variations. Such work remains rare for
42 urban environments, especially megacities. Here, we used near-continuous CO₂ and $\delta^{13}\text{C-CO}_2$
43 measurements, from September 2013 to August 2015, and inverse modeling to constrain the CO₂ budget
44 and investigate the main factors that dominated $\delta^{13}\text{C-CO}_2$ variations for the Yangtze River Delta (YRD)
45 region, one of the largest anthropogenic CO₂ hotspots and densely populated regions in China. We used
46 the WRF-STILT model framework with category-specified EDGAR v432 CO₂ inventories to simulate
47 hourly CO₂ mixing ratios and $\delta^{13}\text{C-CO}_2$, evaluated these simulations with observations, and constrained
48 the anthropogenic CO₂ emission categories. Our study shows that: (1) Top-down and bottom-up estimates
49 of anthropogenic CO₂ emissions agreed well (bias < 6%) on an annual basis; (2) The WRF-STILT model
50 performed well in reproducing the observed diel and seasonal atmospheric $\delta^{13}\text{C-CO}_2$ variations; (3)
51 Anthropogenic CO₂ emissions played a much larger role than ecosystems in controlling the $\delta^{13}\text{C-CO}_2$
52 seasonality. When excluding ecosystem respiration and photosynthetic discrimination in the YRD area,
53 $\delta^{13}\text{C-CO}_2$ seasonality increased from 1.53‰ to 1.66‰; (4) Atmospheric transport processes in summer
54 amplified the cement CO₂ enhancement proportions in the YRD area, which dominated monthly δs
55 variations. These findings support that the combination of long-term atmospheric carbon isotope
56 observations and inverse modeling can provide a powerful constraint on the carbon cycle of these
57 complex megacities.

58 **Keywords:** cements production, ¹³C/¹²C ratio, WRF-STILT model, plants photosynthetic discrimination

59
60
61
62
63
64
65
66
67
68
69
70



71 1. Introduction

72 Urban landscapes account for 70% of global CO₂ emissions and represent less than 1% of Earth's land
73 area (Seto et al., 2014). Such CO₂ hotspots play a dominant role in controlling the rise in atmospheric CO₂
74 concentrations, which exceeded 412 ppm in December 2019 for global monthly average observations
75 (<https://www.esrl.noaa.gov/gmd/ccgg/trends/>). Furthermore, the carbon isotope ratio of CO₂ (i.e. $\delta^{13}\text{C} =$
76 $^{13}\text{C}/^{12}\text{C}$ ratio in delta notation) at the representative Mauna Loa site, USA, has steadily decreased to
77 around -8.5‰, in December 2019 (<https://www.esrl.noaa.gov/>). Anthropogenic CO₂ emission is produced
78 by fossil fuel burning and cement production. As the urban population is expected to increase by 2.5 to 6
79 billion people in 2050, anthropogenic CO₂ emissions are projected to increase dramatically, especially in
80 developing regions and countries (Sargent et al., 2018; Ribeiro et al., 2019). Under such a scenario, the
81 observations of atmospheric CO₂ and $\delta^{13}\text{C}\text{-CO}_2$ in urban landscapes are of great importance to monitoring
82 these potential CO₂ emissions hotspots (Lauvaux et al., 2016; Nathan et al., 2018; Graven et al., 2018;
83 Pillai et al., 2016; Staufer et al., 2016).

84 Countries are required to report their CO₂ emissions according to the Intergovernmental Panel on Climate
85 Change guidelines (IPCC; e.g. IPCC 2013), and many “bottom-up” methods have long been used to
86 estimate CO₂ emissions worldwide, but such methods have high uncertainties for CO₂ emissions at
87 regional (20%) to city (50 to 250%) scales (Gately & Hutyra, 2017; Gately et al., 2015). These significant
88 uncertainties are propagated into the inversion of global biological CO₂ flux (Zhang et al., 2014; Jiang et
89 al., 2014; Thompson et al., 2016). By using CO₂ observations, the “top-down” atmospheric inversion
90 approach is a useful tool to evaluate “bottom-up” inventories (Graven et al., 2018; L. Hu et al., 2019;
91 Lauvaux et al., 2016; Nathan et al., 2018). Previous research has shown that additional information, such
92 as data on atmospheric $\Delta^{14}\text{CO}_2\text{-CO}_2$, $\delta^{13}\text{C}\text{-CO}_2$, and CO, is needed to better distinguish CO₂ emissions
93 from different sources and to assess their uncertainties (Chen et al., 2017; Graven et al., 2018; Nathan et
94 al., 2018; Cui et al., 2019). The use of hourly $\delta^{13}\text{C}\text{-CO}_2$ observation in urban areas remains rare in
95 inversion studies, yet such observations contain invaluable information of anthropogenic CO₂ from
96 different categories.

97 Traditional estimates of $\delta^{13}\text{C}\text{-CO}_2$ using isotope ratio mass spectrometry (IRMS) are very limited because
98 flask air sample collection requires long preparation time and is expensive. Consequently, there is a lack
99 of high temporal and long-term observations of $\delta^{13}\text{C}\text{-CO}_2$ (Sturm et al., 2006). Isotope ratio infrared
100 spectroscopy technology (IRIS) has overcome these limitations. As a result, *in situ* air sample analyses
101 using IRIS analyzers are resulting in dense time series of $\delta^{13}\text{C}\text{-CO}_2$. However, most of the established



102 long-term IRMS and IRIS $\delta^{13}\text{C}$ -CO₂ measurement sites are representative of “background” or natural
103 ecosystem conditions at locations far away from urban landscapes (Chen et al., 2017; Griffis, 2013).

104 To date, long-term (> 1 year) and continuous observations of both CO₂ and $\delta^{13}\text{C}$ -CO₂ have been reported
105 for only five cities, including Bern, Switzerland (Sturm et al., 2006); Boston, USA (McManus et al.,
106 2010); Salt Lake City, USA (Pataki et al., 2006); Beijing, China (Pang et al., 2016); and Nanjing, China
107 (Xu et al., 2017). In these previous investigations, significant diel and seasonal variations of $\delta^{13}\text{C}$ -CO₂
108 have been observed; these patterns were modulated by fossil fuel combustion, plant respiration and
109 photosynthesis, and changes in the height of the atmospheric boundary layer (Sturm et al., 2006; Guha
110 and Ghosh, 2010). No study has quantified the impact of each factor on the seasonal variation of $\delta^{13}\text{C}$ -
111 CO₂. This represents an important knowledge gap in understanding the underlying mechanisms of carbon
112 cycling in complex urban ecosystems.

113 The traditional $\delta^{13}\text{C}$ -CO₂ isotope partitioning methods (including Miller-Tans and the Keeling plot
114 approaches) have been used to constrain different CO₂ sources worldwide (Keeling, 1960; Vardag et al.,
115 2015; Newman et al., 2016; Pang et al., 2016; Xu et al., 2017). These methods are based on the
116 assumption that partitioned atmospheric CO₂ enhancement components from different sources can
117 represent CO₂ emissions at the “target area” (Miller and Tans, 2003; Ballantyne et al., 2011). Carbon
118 dioxide emissions are highly inhomogeneous at the urban scale, with extremely strong point/line sources,
119 and the final partitioning results are highly uncertain without considerations of source footprint
120 characteristics (Gately & Hutrya, 2017; Cui et al., 2019; Martin et al., 2019). Atmospheric transport
121 models can help to resolve such problems, and the coupling of atmospheric transport models with isotope
122 observations have recently been applied in global and regional CO₂ partitioning studies (Chen et al., 2017;
123 Cui et al., 2019; Graven et al., 2018; C. Hu et al., 2018b). Although urban CO₂ inversion has been applied
124 successfully in several studies in Europe and the United States (Bréon et al., 2015; Turnbull et al., 2015;
125 Pillai et al., 2016; Brioude et al., 2013; Turner et al., 2016), urban CO₂ inversions in China are rare
126 (Berezin et al., 2013; C. Hu, 2018a; Worden et al., 2012), presumably because of the scarcity of high
127 quality $\delta^{13}\text{C}$ -CO₂ and CO₂ observations.

128 The Yangtze River Delta (YRD) ranks as one of the most densely populated regions in the world and is
129 an important anthropogenic CO₂ hotspot. Major anthropogenic sources include power industry, oil
130 refineries/transformation and cement productions. Having the largest source of cement-derived CO₂
131 production across China and the world (Cai et al., 2015), the YRD contributed 20% of national cement
132 production, nearly 12% of world’s total cement output in 2014 (Xu et al., 2017; Yang et al., 2017).
133 Besides the anthropogenic factors, natural ecosystems and croplands act as significant CO₂ sinks and
134 sources within the YRD. Independent quantification of the fossil and cement CO₂ emission and



135 assessment of their impact on atmospheric $\delta^{13}\text{C-CO}_2$ have potential to improve our understanding of
136 urban CO_2 cycling. Further, the observations and simulations of both atmospheric CO_2 and $\delta^{13}\text{C-CO}_2$ can
137 help us relate atmospheric CO_2 dynamics with future emissions control strategies.

138 Here, we combine long-term (>2 years) CO_2 and $\delta^{13}\text{C-CO}_2$ observations with atmospheric transport
139 model simulations to study urban atmospheric CO_2 and $\delta^{13}\text{C-CO}_2$ variations. The objectives were to: (1)
140 Constrain anthropogenic CO_2 emissions and determine the main sources of uncertainty for $\delta^{13}\text{C-CO}_2$
141 simulations, and (2) Quantify the relative contributions of each factor (i.e. background, anthropogenic
142 CO_2 emissions especially for cement production, ecosystem photosynthesis and respiration) to seasonal
143 variations of atmospheric $\delta^{13}\text{C-CO}_2$.

144 **2. Materials and methods**

145 **2.1 Observations of atmospheric CO_2 mixing ratio, $\delta^{13}\text{C-CO}_2$ and supporting variables**

146 The observation site is located on the Nanjing University of Information Science and Technology campus
147 (hereafter NUIST, $32^\circ 12' \text{N}$, $118^\circ 43' \text{E}$, green dot in Figure 1a). Continuous atmospheric CO_2 mixing
148 ratios and $\delta^{13}\text{C-CO}_2$ were measured at a height of 34 m above ground with an IRIS analyzer (model
149 G1101-i, Picarro Inc., Sunnyvale, CA). The observation period extended from September 2013 to August
150 2015. Calibrations for CO_2 mixing ratio and $\delta^{13}\text{C-CO}_2$ were conducted with standard gases traceable to
151 NOAA-ESRL (National Oceanic and Atmospheric Administration, Earth System Research Laboratory)
152 standards. Calibration details are provided by Xu et al. (2017). Based on Allan variance analyses, the
153 hourly precisions of CO_2 and $\delta^{13}\text{C-CO}_2$ were 0.07 ppm and 0.05%, respectively.

154 We separated the two-year study period into seasons (autumn: September, October, November; winter:
155 December, January, February; spring: March, April, May; summer: June, July, August). Further, for an
156 annual comparison, we examined the period from September 2013 to August 2014 (Year 2014) versus
157 September 2014 to August 2015 (Year 2015).

158 The YRD is a cement production hotspot in China (Figure 1b). It had a total population of 190 million in
159 2018 (Figure 2a) with 24.2 million in the city of Shanghai, 9.8 million in Hangzhou city (provincial
160 capital of Zhejiang), 8.4 million in Nanjing city (provincial capital of Jiangsu), and 8.1 million in Hefei
161 city (provincial capital of Anhui). The CO_2 related production data (i.e. cement) and energy consumption
162 data (i.e. coal and natural gas) were obtained from local official sources using the same method described
163 in Shen et al. (2014).

164 To examine the effects of plant photosynthesis on atmospheric CO_2 variations, we used NDVI
165 (Normalized Difference Vegetation Index), SIF (solar-induced chlorophyll fluorescence) and GPP (gross



166 primary productivity) information. These three products have a global distribution with spatial resolution
167 of 0.05° by 0.05° . The NDVI has a temporal resolution of 16 days and SIF and GPP products have a
168 temporal resolution of 8 days (Li & Xiao, 2019; <http://globalecology.unh.edu/data/>). Land-use and land-
169 cover classification in Yangtze River Delta for 2014 was applied by using NDVI data of MOD13A2.

170 2.2 Simulation of atmospheric $\delta^{13}\text{C-CO}_2$

171 2.2.1 General equations

172 The simulation of atmospheric $\delta^{13}\text{C-CO}_2$ is based on mass conservation. First, we briefly describe the
173 simulation of atmospheric CO_2 mixing ratios (more details are provided in Section 2.2.2), following the
174 previous work of Hu et al., (2018b), where CO_2 was simulated as the sum of background (CO_{2_bg}) and the
175 contribution from all regional sources/sinks (ΔCO_2), as

$$176 \quad \text{CO}_{2_ms} = \text{CO}_{2_bg} + \Delta\text{CO}_2 \quad (1)$$

177 Based on mass conservation, we estimated the $^{13}\text{CO}_2$ composition by multiplying the left and right hands
178 of equation (1) by $\delta^{13}\text{C}$,

$$179 \quad \delta^{13}\text{C}_a = \frac{\delta^{13}\text{C}_{bg} \times \text{CO}_{2_bg} + \sum_{i=1}^n \delta_i^{13} \times [\Delta\text{CO}_2]_i}{\text{CO}_{2_ms}} \quad (2)$$

180 where $\delta^{13}\text{C}_a$ and $\delta^{13}\text{C}_{bg}$ represent the atmospheric $\delta^{13}\text{C-CO}_2$ and background $\delta^{13}\text{CO}_2$, δ_i^{13} is the $\delta^{13}\text{C-CO}_2$
181 for end-member i (including anthropogenic and biological source categories). The $\delta^{13}\text{C-CO}_2$ contributions
182 from all regional sources/sinks can be further reformatted as equation 3,

$$183 \quad \sum_{i=1}^n \delta_i^{13} \times [\Delta\text{CO}_2]_i = \delta_s \times \Delta\text{CO}_2 \quad (3)$$

184 where δ_s is the mixture of all regional end-members (Newman et al., 2008), which will be described in
185 detail in section 2.2.5, and ΔCO_2 represents the sum of CO_2 mixing ratio from all regional contributions
186 (hereafter total CO_2 enhancement). The product of $\delta_s \times \Delta\text{CO}_2$ can be treated as the regional source term.

187 To date, there are no available global $\delta^{13}\text{C-CO}_2$ background products and the choice of $\delta^{13}\text{C}_{bg}$ is essential
188 to simulating $\delta^{13}\text{C}_a$. Here, we apply three strategies. First, we used discrete $\delta^{13}\text{C-CO}_2$ flask observations
189 at Mount Waliguan (hereafter WLG, $36^\circ 17' \text{N}$, $100^\circ 54' \text{E}$; <https://www.esrl.noaa.gov/gmd/dv/data/>) to
190 represent the $\delta^{13}\text{C-CO}_2$ background signal at our site. These observations were measured at weekly
191 intervals to the end of 2015. A digital filtering curve fitting (CCGCRV) regression method was applied to



192 derive hourly background values following Thoning et al. (1989). There are, however, reasons why WLG
193 may not be an ideal background site for our study domain. For example, based on the previous simulation
194 results for the CO₂ background sources, background air masses should originate from the free atmosphere
195 at heights of 1000 m or higher above the ground (Hu et al., 2019). Here, the WLG observations were
196 made near the surface. Further, WLG is not located at the border of our simulation domain 1. Therefore,
197 the strong vertical $\delta^{13}\text{C-CO}_2$ gradients between the boundary layer and the free tropospheric atmosphere
198 (Chen et al., 2006; Guha et al., 2010; Sturm et al., 2013) can cause a high bias in the $\delta^{13}\text{C-CO}_2$
199 background when using this approach.

200 In the second approach, the $\delta^{13}\text{C-CO}_2$ background signal was estimated with wintertime “clean” air CO₂
201 and $\delta^{13}\text{C-CO}_2$ observations at the NUIST site, using the following equation

$$202 \quad \delta^{13}\text{C}_{bg} = \frac{\delta^{13}\text{C}_a \times [\text{CO}_2] - \sum_{i=1}^n \delta_i^{13} \times [\Delta\text{CO}_2]_i}{\text{CO}_{2_bg}} \quad (4)$$

203 where $\delta^{13}\text{C}_a$ and $[\text{CO}_2]$ represent atmospheric $\delta^{13}\text{C-CO}_2$ and CO₂ observations at the NUIST site under
204 clean conditions. $[\Delta\text{CO}_2]_i$ is the simulated category-specified CO₂ enhancement. Here, we defined clean
205 conditions as the lowest 5% quintile wintertime CO₂ observations to minimize simulated CO₂
206 enhancement errors on $\delta^{13}\text{C-CO}_2$ background calculation. The CO_{2_{bg}} is obtained from heights 1000 m
207 above ground level (see Section 2.2.3).

208 In the third approach, we avoid the use of modeled $[\Delta\text{CO}_2]_i$ results and replaced the regional source term
209 in equation 4 with $\delta\text{s} \times \Delta\text{CO}_2$, as described in equations 3, and used the Miller-Tans regression method to
210 calculate monthly δs . This approach does not require simulation of $[\Delta\text{CO}_2]_i$ or the corresponding $\delta^{13}\text{C-}$
211 CO₂ signals. The hourly $\delta^{13}\text{C-CO}_2$ background value can be derived by using δs , CO₂ background,
212 observed atmospheric $\delta^{13}\text{C}_a$ and CO₂ (see details in Section 2.3 and supplement materials). Comparison of
213 these three strategies will be evaluated and discussed in Section 3.2.1. Similar methods used to derive
214 other background tracers have been used including CO₂ (Alden et al., 2016; Verhulst et al., 2017), CO
215 (Wang et al., 2010; Ruckstuhl et al., 2012) and CH₄ (Zhao et al., 2009; Verhulst et al., 2017; Hu et al.,
216 2019). To analyze the controlling factors for the $\delta^{13}\text{C-CO}_2$ seasonality, the CCGCRV regression was
217 applied to the background, observations, and simulations. Finally, we derived CCGCRV curving fitting
218 lines and defined the difference between peak and trough in one year as the seasonality of $\delta^{13}\text{C-CO}_2$.

219 **2.2.2 Simulation of atmospheric CO₂ mixing ratios**



220 In equation 1, the CO_{2_bg} is obtained from the Carbon Tracker 2016 product, which provides global CO_2
221 distributions from the ground level up to a height of 50 km. We used the concentration at a height of 1000
222 m above ground where the air mass enters study domain 1 (Figure 1a). The variable ΔCO_2 was derived by
223 multiplying the simulated hourly footprint function with the CO_2 fluxes (see details in Sect. 2.2.4). The
224 CO_2 fluxes contain anthropogenic CO_2 emissions, biological CO_2 flux and biomass burning. Here the
225 anthropogenic CO_2 emission sources include power industry, combustion for manufacturing, non-metallic
226 minerals production (cement), oil refineries/transformation industry, energy for building and road
227 transportation. Theoretically, ΔCO_2 represents the CO_2 changes contributed by every pixel within the
228 simulated domain. As shown by Hu et al. (2018a), most of the ΔCO_2 is contributed by sink/source
229 activity within the YRD area. In order to quantify the relative contributions within the YRD area, we
230 separated the study domain into 5 zones based on provincial administrative boundaries including Jiangsu,
231 Anhui, Zhejiang, Shanghai, and the remaining area outside the YRD. The modeled CO_2 was calculated as
232 follows:

$$233 \quad \Delta CO_2 = \sum_{i=1}^n flux_i \times footprint \quad (5)$$

234 where $flux_i$ corresponds to each CO_2 flux category simulated for each domain, and footprint is the model
235 simulated sensitivity of observed CO_2 enhancement to flux changes in each pixel as described below.

236 2.2.3 WRF-STILT model configuration

237 The Stochastic Time-Inverted Lagrangian Transport (hereafter STILT) model was used to generate the
238 above footprint, which is defined as the sensitivity of atmospheric CO_2 enhancement to the upwind flux at
239 the receptor site (observation site). The meteorological fields used to drive the STILT model were
240 simulated with the Weather Research and Forecasting Model (WRF3.5) at high spatial and temporal
241 resolutions. The innermost nested domain (D3, 3 km \times 3 km, Figure 1) contains the YRD area, where the
242 most sensitive footprint is located, and the intermediate domain (D2, 9 km \times 9 km) and outermost (D1, 27
243 km \times 27 km) represent East China and Central and Eastern China, respectively. The WRF setup used
244 physical schemes and parameters that have been used previously for inverse analyses (Hu et al., 2019).
245 These previous studies at the NUIST observation site have shown very good performance in simulating
246 the meteorological fields, which is essential for reliable STILT simulations. The hourly footprint was
247 simulated by releasing 500 particles from the NUIST measurement site and tracking their locations every
248 5 minutes for a period of 7 days. Particle numbers and their residence time within half of the planetary
249 boundary layer (hereafter PBL) height were used to calculate the footprint over the 7 day period. For the
250 CO_2 background of each hour, we tracked the sources of air particles back trajectory at the end of 7 days



251 at the heights above 1000 m, and defined these CO₂ mixing ratios in Carbon Tracker as the hourly CO₂
252 background values (Peters et al., 2007).

253 **2.2.4 A priori anthropogenic CO₂ emissions and net ecosystem exchange**

254 The Emission Database for Global Atmospheric Research (EDGAR) inventory was selected as the *a*
255 *priori* anthropogenic CO₂ emissions (Figure 2a), which is based on the International Energy Agency's
256 (IEA) energy budget statistics and provides detailed CO₂ source maps (19 categories, including both
257 organic and fossil emissions, IEA, 2012) with global coverage at high spatial resolution (0.1° × 0.1°). The
258 EDGAR CO₂ emissions are the most up-to-date global inventory (Janssens-Maenhout et al., 2017;
259 Schneising et al., 2013). Other inventories, including the Fossil Fuel Data Assimilation System (FFDAS,
260 Rayner et al., 2010) and the Open-source Data Inventory for Anthropogenic CO₂ (ODIAC, Oda et al.,
261 2018) also provide global CO₂ emissions. However, these inventories only provide total CO₂ emissions or
262 have very limited emission categories, which limit our ability to provide isotope end-member information.
263 EDGAR v432 provides emission estimates at a monthly time scale. Here, we applied hourly scaling
264 factors for different categories following Hu et al., (2018a). EDGAR v432 is available only for 2010. We
265 assume that each CO₂ category changes linearly from its 2010 value (Peters et al., 2007) and apply an
266 annual scaling factor of 1.145 to derive CO₂ emissions for 2014 and 2015. This scaling factor is based on
267 Carbon Tracker anthropogenic CO₂ emissions for YRD.

268 The biological flux or net ecosystem CO₂ exchange (NEE) and biomass burning CO₂ emissions come
269 from Carbon Tracker *posteriori* flux at 3-hour intervals and at a spatial resolution of 1° × 1°. Because
270 NEE is much smaller than the anthropogenic CO₂ emissions in such densely developed urban landscapes,
271 we homogeneously distributed this flux at a spatial resolution of 0.1° within each grid to match the
272 footprint.

273 **2.2.5 The simulation of carbon isotope ratio of all sources (δs)**

274 The carbon isotope ratio of all the surface sources was calculated as (Newman et al., 2008):

$$275 \quad \sum_{i=1}^n \delta_i \times p_i = \delta_s \quad (6)$$

276 where δ_i is the $\delta^{13}\text{C-CO}_2$ value from source category i , and p_i is the corresponding enhancement
277 proportion. Based on fossil fuel usage characteristics in YRD, we reassigned the EDGAR v432 categories
278 according to fuel types. Coal was the fuel type for manufacturing, oil for oil refinery, natural gas for
279 buildings, and diesel and gasoline for transportation. The power industry consumed 5% natural gas and 95%



280 coal based on local activity data in YRD (China statistical Yearbook, 2015). The non-metallic mineral
281 production was mainly for cement. Chemical processes were mainly ammonia synthesis. Based on a
282 literature review and our previous work (Xu et al., 2017), typical $\delta^{13}\text{C}\text{-CO}_2$ values for natural gas (-39.06‰
283 $\pm 1.07\text{‰}$), coal ($-25.46\text{‰} \pm 0.39\text{‰}$), fuel oil ($-29.32\text{‰} \pm 0.15\text{‰}$), gasoline ($-28.69\text{‰} \pm 0.50\text{‰}$),
284 ammonia synthesis ($-28.18\text{‰} \pm 0.55\text{‰}$), and diesel ($-28.93\text{‰} \pm 0.26\text{‰}$), pig iron ($-24.90\text{‰} \pm 0.40\text{‰}$),
285 crude steel ($-25.28\text{‰} \pm 0.40\text{‰}$), cement ($0\text{‰} \pm 0.30\text{‰}$), biological and organic emissions ($-28.20\text{‰} \pm$
286 1.00‰) were used in this study. We also applied a value of -28.20‰ for photosynthesis (Griffis et al.,
287 2008; Lai et al., 2014) because YRD is a region dominated by C_3 plants.

288 To evaluate the simulated δ_s , we applied the Miller-Tans and Keeling plot approaches to derive δ_s from
289 the observed concentration and atmospheric $^{13}\text{CO}_2\text{-CO}_2$ (Xu et al. 2017). We then used the results to
290 evaluate the calculations made with Equation (6).

291 **2.3 Independent IPCC method for anthropogenic CO_2 emissions**

292 Large differences between different inventories have been previously found even for the same region
293 (Berezin et al., 2013; Andrew, 2019). For comparison with the EDGAR v432 inventory results, we
294 derived the anthropogenic CO_2 emissions by using an independent IPCC method. Here, we illustrate the
295 calculation for cement CO_2 emissions. Note that the IPCC only recommended an EF for clinker, which is
296 an intermediate product of cement. To calculate cement CO_2 emissions, we need to calculate it based on
297 clinker production, as shown in Equation (7),

$$298 \quad \text{CO}_2[\text{cement}] = M_{\text{cement}} \times C_{\text{clinker}} \times \text{EF}_{\text{clinker}} \quad (7)$$

299 where $\text{CO}_2[\text{cement}]$ is the chemical process CO_2 emissions for cement production, M_{cement} is the
300 production of cement, C_{clinker} represents the clinker to cement ratio (%), and $\text{EF}_{\text{clinker}}$ is the CO_2 emission
301 factor for clinker production. The IPCC recommended an $\text{EF}_{\text{clinker}}$ value of 0.52 ± 0.01 tonne CO_2 per
302 tonne clinker produced, where CaO content for clinker is assumed to be 65% with 100% CaO from
303 calcium carbonate material (IPCC 2013). The EF appears to be well constrained, showing little variation
304 among provinces with mean values ranging from 0.512 to 0.525 (Yang et al., 2017). For the C_{clinker} values,
305 it generally showed a decreasing trend from 64.5% in 2004 to 56.9% in 2015 for all of China (Figure S1),
306 with an average value of 57.0% during 2014 and 2015.

307 **2.4 Multiplicative scaling factor method**

308 To quantify anthropogenic CO_2 emissions and to compare it with EDGAR products, we first derived the
309 monthly scaling factors for anthropogenic CO_2 emissions using a multiplicative scaling factor (hereafter



310 MSF) method (Hu et al., 2019; Sargent et al., 2018; He et al., 2020), and then obtained annual averages.
311 The monthly scaling factors (SFs) were calculated as:

$$312 \quad MSF = \frac{CO_{2_obs} - CO_{2_bg} - \Delta CO_{2_bio} - \Delta CO_{2_fire}}{\Delta CO_{2_ms}} \quad (8)$$

313 where CO_{2_obs} , ΔCO_{2_bio} , ΔCO_{2_fire} and ΔCO_{2_ms} represent observed CO_2 mixing ratios, simulated CO_2
314 enhancements contributed by biological flux, biomass burning and anthropogenic emissions, respectively.
315 Uncertainties of all factors on the final MSFs were calculated based on Monte Carlo methods, where the
316 normal sample probability distribution was applied and the upper 97.5% and lower 2.5% of the values
317 was considered as the uncertainty for MSF (Cao et al., 2016).

318 **3. Results and Discussion**

319 **3.1 Evaluation of hourly CO_2 mixing ratios**

320 **3.1.1 Hourly and monthly CO_2 mixing ratio comparisons**

321 This section examines the general performance of simulating hourly CO_2 mixing ratios. The two-year
322 average hourly footprint is shown in Figure 2b where the source area (blue) indicates strong sensitivity of
323 the CO_2 observations to regional sources. This footprint shape is representative of the YRD area. To
324 quantify the relative contributions from each province, we calculated CO_2 enhancements contributed by
325 Anhui, Jiangsu, Zhejiang, Shanghai, and the remaining area outside of the YRD, respectively. The results
326 indicate that Jiangsu contributed approximately 80% of the total enhancement (discussed further in
327 Section 3.1.2). Comparisons between simulated and observed hourly CO_2 mixing ratios are displayed in
328 Figure 3a for both years. For all hourly data in each year, the model versus observation correlation
329 coefficient (R) was $R = 0.38$ ($n = 8204$, $P < 0.001$) and $RMSE = 29.44$ ppm for 2014, and $R = 0.35$ ($n =$
330 7262 , $P < 0.001$) and $RMSE = 30.22$ ppm for 2015. These results indicate that the model can simulate the
331 synoptic and diel CO_2 variations over the two-year period. The model also performed well in simulating
332 the monthly and seasonal variations of CO_2 mixing ratios (daily averages are shown in Figure S2). The
333 simulations captured the trend of rising CO_2 mixing ratios after October and the drawdown of CO_2 below
334 the background value during the summer.

335 Figures 3b-d illustrate the average monthly daily, nighttime, and daytime CO_2 mixing ratios. These
336 monthly values contain the effects including atmospheric transport, background fields and variations in
337 CO_2 emissions. The observed and simulated CO_2 mixing ratios showed a significant increase from
338 September 2013 to January 2014. Here, the CO_2 mixing ratios increased by 16.0 ppm according to the
339 model results and 17.2 ppm according to the observations. The background values increased by 8.1 ppm
340 and accounted for 47% of the total CO_2 increase, and the net CO_2 flux (*a priori*) for YRD increased by



341 15%. We attributed the remaining 38% increase to changes in atmospheric transport processes including
342 lower PBL heights in January 2014 than in September 2013. To quantify how variations in PBL height
343 affected CO₂ mixing ratios, we compared the simulated monthly anthropogenic CO₂ enhancement
344 differences in the same months of different years, to eliminate the influence of monthly emission
345 variations on CO₂ enhancements. Twelve monthly paired values were used and are shown in Figure 4a.
346 This analysis indicates that atmospheric CO₂ mixing ratios decreased by about 3.7 ppm for an increase of
347 PBL height by 100 m.

348 On an annual timescale, the simulated average CO₂ mixing ratios were 436.63 ppm and 437.11 ppm for
349 2014 and 2015, respectively. Since the anthropogenic CO₂ emissions used in the model are the same for
350 both years, the simulated annual average CO₂ difference can be used to quantify the influence associated
351 with meteorological factors and ecosystem carbon cycling. Between these two years, the CO₂ background
352 increased by 1.78 ppm, the biological enhancement decreased by 1.04 ppm from 2014 to 2015. The
353 remaining 0.26 ppm change between 2014 and 2015 indicates a relatively small meteorological effect,
354 such as a slight change in dominant wind direction or a PBL height difference.

355 The simulated annual average NEE CO₂ enhancements were 2.64 ppm and 1.60 ppm for the respective
356 years. For comparison, the annual average anthropogenic enhancements were 36.20 ppm and 34.90 ppm
357 for 2014 and 2015, respectively. The monthly NEE enhancement varied from -0.1 ppm in May 2015 to
358 +6.0 ppm July 2014, indicating NEE contributes positively for enhancement in most months (Figure 5a),
359 even though the sign of monthly averaged NEE flux in summer was negative (sinks). This positive
360 contribution was mainly caused by diel PBL height variations between daytime (smaller negative
361 enhancement) and nighttime (larger positive enhancement). To further evaluate the impact of plant
362 photosynthetic activity on the regional CO₂ cycle, we examined the NDVI, SIF and GPP seasonal patterns
363 (Figures 4b-c). These three datasets revealed two peaks during each year, which is related to increased
364 photosynthetic activity. The first peak occurred in May and the second in August-September,
365 corresponding to the growing season of wheat and corn/rice, respectively (Deng et al., 2015). The land-
366 use classification in YRD for 2014 (Figure S3) shows that north YRD is dominated by agricultural land
367 and south dominated by forest land, and our observation site was more surrounded by agricultural land
368 which corresponded well with observed NDVI, SIF and GPP seasonal patterns. The peak SIF and GPP
369 signals during the summer were about 20 times greater than during the winter. Consequently, we can
370 ignore the potential influence of photosynthetic activity on the regional CO₂ enhancements during the
371 non-growing seasons.

372 3.1.2 Components of urban CO₂ enhancement



373 Here, we diagnose the source contributions to the urban CO₂ enhancement. The observed anthropogenic
374 CO₂ enhancements, which were derived by subtracting CO₂ background and simulated biological
375 enhancement from CO₂ concentration observations, were 38.36 ppm and 37.89 ppm for 2014 and 2015,
376 respectively. The corresponding simulated anthropogenic CO₂ enhancements were 36.20 ppm and 34.90
377 ppm. In comparison with the simulated biological CO₂ enhancements displayed in Figure 5a, both the
378 observed and simulated CO₂ enhancements are indicative of a large anthropogenic (fossil fuel and cement
379 production) CO₂ emission from the YRD.

380 Previous studies have also investigated urban CO₂ enhancements from a relatively broad range of
381 developed environments worldwide. Verhulst et al. (2017) measured CO₂ mixing ratios at seven sites in
382 Los Angeles, USA and concluded that the mean annual enhancement varied between 2.0 ppm and 30.8
383 ppm, which is considerably lower than our findings. Another study in Washington, USA in February and
384 July 2013 showed that the CO₂ enhancement was less than 20 ppm (Mueller et al., 2018). The urban CO₂
385 observations and modeling study by Martin et al. (2019) at three urban sites in Eastern USA showed an
386 enhancement of ~21 ppm in February 2013, substantially lower (by ~20 ppm) than our observations. The
387 measurements at an urban-industrial complex site in Rotterdam, Netherlands, indicated a CO₂
388 enhancement of only 11 ppm for October to December 2014 (Super et al., 2017). Our enhancements were
389 significantly higher than all of these previous reports, indicating greater anthropogenic CO₂ emissions
390 than other urban areas.

391 The anthropogenic components and source area contributions are displayed in Figure 5b-c. During the
392 study period the average anthropogenic enhancements were 5.1%, 80.2%, 1.9%, 4.4%, and 8.5% for
393 Anhui, Jiangsu, Zhejiang, Shanghai, and the remaining area outside the YRD, respectively. Although
394 Shanghai's area is the smallest within the YRD region and relatively distant (~300 km) from our
395 observation site, its maximum source contribution at times exceeded 50% (i.e. on 19th September 2013)
396 *via* long-distance transport. In general, power industry, manufacturing, non-metallic mineral production,
397 oil refinery, and other source categories contributed 41.0%, 21.9%, 9.3%, 11.5%, and 16.3% to the total
398 anthropogenic CO₂ enhancement, respectively. The proportions of corresponding CO₂ emission
399 categories to the total anthropogenic emissions of the YRD were 39.8%, 28.4%, 7.4%, 4.1%, and 24.4%,
400 respectively. We found a relatively large difference between the enhancement proportion and the
401 emission proportion for oil refinery (from 11.5% to 4.1%) as compared to other categories. This may be
402 because power industry, manufacturing and non-metallic mineral production were more homogeneously
403 distributed than oil refinery, and oil refinery activities were closer to our CO₂ observation site.

404 **3.1.3 Constraints on monthly anthropogenic CO₂ emissions**



405 To provide a robust comparison of bottom-up CO₂ emissions for YRD, we calculated anthropogenic CO₂
406 emissions from both EDGAR v432 and with activity data provided by local governments (Table 1) and
407 the default IPCC emission factors (<https://www.ipcc-nggip.iges.or.jp/EFDB/>). The total anthropogenic
408 CO₂ emissions in 2014 were 2.44×10^{12} kg and 2.35×10^{12} kg according to our own inventory and
409 EDGAR v432 CO₂, respectively, indicating excellent agreement (within 4%) between these approaches.
410 We constrained the monthly anthropogenic CO₂ emissions by using the MSF method (equation 8) and
411 computed the 12-month average to represent the years of 2014 and 2015. The *posteriori* results indicate
412 that the annual scaling factors were 1.03 ± 0.10 for 2014 and 1.06 ± 0.09 for 2015. The anthropogenic
413 CO₂ emissions in year 2015 did not show a significant change compared to 2014, and the overall
414 estimates were within the uncertainty of the estimates. After applying the average scaling factors for 2014
415 and 2015, the *posteriori* anthropogenic CO₂ emissions were $2.46 (\pm 0.24) \times 10^{12}$ kg for YRD area. The
416 application of the MSF method provides an overall constraint on the anthropogenic CO₂ emissions. As
417 noted, cement CO₂ emissions in the YRD is the largest regional source for global cement production (also
418 displayed in Table 1).

419 3.2 Simulation of atmospheric $\delta^{13}\text{C-CO}_2$

420 3.2.1 Background atmospheric $\delta^{13}\text{C-CO}_2$

421 To obtain the best representative $\delta^{13}\text{C-CO}_2$ background value for the study domain we examined the
422 values from the three strategies described above (Figure 6). We also compared the $\delta^{13}\text{C-CO}_2$ at the WLG
423 background site with observations at NUIST during winters (Figure S4). This was performed to help
424 simplify the comparison by removing the effects of plant photosynthetic discrimination. The $\delta^{13}\text{C-CO}_2$ at
425 the WLG site was relatively more depleted in the heavy carbon isotope (or negative, by up to 0.5‰) than
426 that observed at NUIST for many periods. Theoretically, there are two key factors that can cause the
427 urban atmospheric $\delta^{13}\text{C-CO}_2$ to be relatively more enriched in the heavy carbon isotope (or positive)
428 compared to the background values including: 1) Discrimination associated with ecosystem
429 photosynthesis; and 2) Discrimination associated with the CO₂ derived from cement production. As
430 shown earlier, the biological CO₂ enhancement was positive in winter, which implies a negligible role of
431 plants photosynthesis. Further, sensitivity tests for cement CO₂ sources showed its influence is much
432 smaller than observed difference in Figure S4 (discussed in section 3.3.3). Based on the above analyses
433 and methods introduced in Section 2.3, we concluded that WLG $\delta^{13}\text{C-CO}_2$ is not an ideal choice for the
434 domain. The wintertime $\delta^{13}\text{C-CO}_2$ background values, based on strategy 2, were -7.78‰ and -7.61‰ for
435 2013-2014 and 2014-2015, respectively. The corresponding values, based on strategy 3, were -7.70‰ and
436 -7.53‰. These background values are more enriched compared to the WLG observations by 0.80‰ to
437 1.01‰. These derived backgrounds agree well with the monthly PBL $\delta^{13}\text{C-CO}_2$ simulation results of



438 Chen et al. (2006) who showed that $\delta^{13}\text{C-CO}_2$ is 0.6‰ higher above the PBL than in the surface layer
439 near the ground. Recently, Ghasemifard et al. (2019) showed that hourly $\delta^{13}\text{C-CO}_2$ values at Mount
440 Zugspitze, the highest (2650 m) mountain in Germany, were about -7‰ in the winter for 2013. During an
441 especially clean air event (10 days in October) at Mount Zugspitze, the average $\delta^{13}\text{C-CO}_2$ was
442 approximately -7.5‰, which is consistent with our estimates using strategies 2 and 3. Based on the
443 evidence presented above, we believe that strategy 3 is the most robust way to derive a background $\delta^{13}\text{C-}$
444 CO_2 for the domain.

445 3.2.2 Evaluation of $\delta^{13}\text{C-CO}_2$ simulations

446 Figure 7a shows the hourly $\delta^{13}\text{C-CO}_2$ simulations over a two-year period. To the best of our knowledge,
447 this is the first time that $\delta^{13}\text{C-CO}_2$ has been simulated at an hourly time scale for an urban region. The
448 simulations are consistent with the observations at daily, monthly and annual time scales, where the
449 average value of observations (simulations) were -8.69‰ (-8.68‰) and -8.52‰ (-8.45‰) for 2014 and
450 2015, respectively. The corresponding correlation was $R = 0.54$ ($P < 0.001$) and $R = 0.52$ ($P < 0.001$).
451 The root mean square error between observations and simulations was 1.07‰ for 2014 and 1.10‰ for
452 2015 (Table 2). Further, the observed and simulated $\delta^{13}\text{C-CO}_2$ values showed seasonal variations that
453 increased in summer and decreased in winter. This pattern mirrored the CO_2 mixing ratios for both
454 observations and simulations (Figures 3 and 7). Similar relations and seasonal variations of $\delta^{13}\text{C-CO}_2$
455 have been reported in other urban areas (Sturm et al., 2006; Guha & Ghosh, 2010; Moore & Jacobson,
456 2015; Pang et al., 2016). The simulated hourly NEE CO_2 enhancement is also shown in Figure 7b. Note
457 that negative values indicate net CO_2 sinks and positive values indicate net CO_2 sources. We can see large
458 hourly variations in the growing seasons and positive enhancements during nighttime that are generally
459 larger than negative enhancements during daytime. This shows the potential influence of NEE on $\delta^{13}\text{C-}$
460 CO_2 seasonality. To date, no study has quantified the relative contributions to the $\delta^{13}\text{C-CO}_2$ seasonality.
461 Here, we re-evaluate and quantify the main factors contributing to its seasonality based on the
462 combination of $\delta^{13}\text{C-CO}_2$ observations and simulations in the following section.

463 Here, we examine the comparisons for winter and summer in greater detail. The simulations showed that
464 the model can generally capture the diel variations of observed hourly $\delta^{13}\text{C-CO}_2$ variations (Figure 8).
465 Statistics between observations and simulations for two seasons are shown in Table 2. The observed
466 seasonal average significantly increased, by 1.18‰, from winter 2013-2014 (-9.27‰) to summer 2014 (-
467 8.09‰). The simulations showed a similar seasonal increase of 1.35‰. Some large discrepancies are
468 evident and generally caused by the simulated total CO_2 enhancement biases and the negative relationship
469 between $\delta^{13}\text{C-CO}_2$ and the CO_2 enhancement.



470 Comparisons between observations and simulations for daily average CO₂ mixing ratio and $\delta^{13}\text{C-CO}_2$ are
471 also shown in Figure 9. Although the data are distributed around the 1:1 line for both seasons, there is less
472 scatter and higher correlation in the winter than in the summer. We attributed this to the more complex
473 biological CO₂ sinks in the summer, which are not adequately resolved by the relatively coarse model
474 grid (1° by 1°).

475 3.2.3 Mechanisms controlling the $\delta^{13}\text{C-CO}_2$ seasonality

476 The mechanisms driving these seasonal variations are examined below. The peak and trough in the
477 observed $\delta^{13}\text{C-CO}_2$ signal was observed in December and July, respectively, yielding an amplitude of
478 1.51‰. This was consistent with the simulated amplitude of 1.53‰. These results support that the
479 simulated $\delta^{13}\text{C-CO}_2$ seasonality agreed well with the observations (Figure 10), and can be used to further
480 diagnose the mechanisms contributing to the $\delta^{13}\text{C-CO}_2$ seasonality. According to equation 2, the $\delta^{13}\text{C-}$
481 CO₂ seasonality can be attributed to four factors including: (1) A change in the background $\delta^{13}\text{C-CO}_2$
482 value from -7.64‰ in December to -6.66‰ in July; (2) A change in CO₂ background from 399 ppm to
483 398 ppm; (3) The total CO₂ enhancement change from 45.7 ppm to 37.3 ppm; and (4) The change in the
484 isotope composition of the CO₂ enhancements causing δs to vary from -26.1‰ to -22.8‰.

485 To quantify each mechanism's contribution to the seasonality of atmospheric $\delta^{13}\text{C-CO}_2$, we recalculated
486 $\delta^{13}\text{C-CO}_2$ by using the monthly averages as described above. First, we calculated $\delta^{13}\text{C-CO}_2$ in December
487 and July, which were -9.54‰ and -8.04‰, respectively, with amplitude of 1.50‰. Next, we replaced the
488 $\delta^{13}\text{C-CO}_2$ background value in December (-7.64‰) with July (-6.67‰). The recalculated $\delta^{13}\text{C-CO}_2$ was -
489 8.66‰ in December, indicating that the change in $\delta^{13}\text{C-CO}_2$ background value caused a change of 0.88‰
490 (9.54‰ minus -8.66‰) to the seasonality. By changing both the total CO₂ enhancement and background
491 values, the recalculated $\delta^{13}\text{C-CO}_2$ was -8.32‰, contributing a 0.34‰ change in the seasonality (-8.66‰
492 minus -8.32‰). Finally, by changing δs from -26.1‰ to -22.8‰, together with the change in background
493 value, the recalculated $\delta^{13}\text{C-CO}_2$ was -8.32‰ – a change of 0.34‰ (i.e. -8.66‰ minus -8.32‰). This
494 indicates that both the total CO₂ enhancement and change in δs contributed equally to the regional source
495 term, causing a variation of 0.62‰ (i.e. 1.50‰ minus 0.88‰). Based on the above analyses, we attributed
496 59% and 41% of the $\delta^{13}\text{C-CO}_2$ seasonality to the changing $\delta^{13}\text{C}$ background term and regional source
497 terms, respectively. Further, the total CO₂ enhancement and CO₂ enhancement components contributed
498 equally (about 20%) to the $\delta^{13}\text{C-CO}_2$ seasonality.

499 To investigate how ecosystem photosynthetic discrimination and respiration affected atmospheric $\delta^{13}\text{C-}$
500 CO₂ seasonality, we simulated the $\delta^{13}\text{C-CO}_2$ again for two cases: (1) excluding photosynthetic
501 discrimination, and (2) excluding both photosynthetic discrimination and respiration. Note that only NEE



502 was used in our study with no partitioning between photosynthesis and respiration in the daytime.
503 Hereafter, we use negative NEE to define case 1 when photosynthesis exceeded respiration. The results
504 are shown in Figure 10 b-c. Overall, the negative CO₂ enhancement (i.e. photosynthesis > respiration)
505 caused atmospheric $\delta^{13}\text{C-CO}_2$ to become more enriched than the baseline simulations with maximum
506 values around 1‰ between April and October (Figure 10b), and positive CO₂ enhancement (i.e. via
507 respiration) caused atmospheric $\delta^{13}\text{C-CO}_2$ to become more depleted compared to the baseline simulations
508 through the whole year (Figure 10c). By applying the CCGRCV fitting technique to the $\delta^{13}\text{C-CO}_2$ for the
509 above two cases, we found that the $\delta^{13}\text{C-CO}_2$ seasonality decreased to 1.45‰ in case 1, indicating
510 ecosystem photosynthetic discrimination explained only 0.08‰ of the seasonality (1.53‰ minus 1.45‰).
511 For case 2, the $\delta^{13}\text{C-CO}_2$ trough in winter slightly increased by 0.08‰ and peak in summer increased by
512 0.20‰, these two factors finally lead the seasonality increase to 1.66‰, which were caused by much
513 larger respiration CO₂ enhancement in summer than in winter (Figure 7b). These results indicate that
514 biological respiration reduced the $\delta^{13}\text{C-CO}_2$ seasonality by 0.20‰, and that negative NEE (photosynthetic
515 discrimination) acted to increase the $\delta^{13}\text{C-CO}_2$ seasonality by 0.08‰. Generally, ecosystem
516 photosynthesis played a minor role in controlling the atmospheric $\delta^{13}\text{C-CO}_2$ seasonality within this urban
517 area. In other words, the anthropogenic CO₂ emissions played a much larger role than the plants.

518 As shown in Figure 5, CO₂ sources from power industry, combustion for manufacturing, non-metallic
519 mineral production and oil refineries and transformation industry were the top 4 contributors to the CO₂
520 enhancements. We simulated atmospheric $\delta^{13}\text{C-CO}_2$ by assuming that no CO₂ was emitted from each of
521 these 4 categories. The simulations were performed by excluding one category at a time. The results
522 indicated that atmospheric $\delta^{13}\text{C-CO}_2$ seasonality was 1.30‰, 1.57‰, 1.30‰, and 1.47‰, if excluding
523 power industry, combustion for manufacturing source, oil refineries/transformation industry, and non-
524 metallic mineral production sources, respectively. In other words, power industry and oil refineries/
525 transformation industry together contributed a 0.40‰ to the total regional source term of 0.62‰. The
526 cement sources played a role in enriching (0.05‰ to 0.07‰) the atmospheric $\delta^{13}\text{C-CO}_2$ in the heavy
527 isotope, contrary to all other anthropogenic CO₂ sources.

528 3.3 Sensitivity analysis

529 3.3.1 Comparison of $\delta\text{s}\cdot\Delta\text{CO}_2$

530 Based on equation 2, the regional source term determines the hourly/daily variations of $\delta^{13}\text{C-CO}_2$, which
531 is treated as a signal added to the background signal. To evaluate the model simulated regional source
532 term with respect to the observations we examined daily averages for winter to minimize the influence of
533 photosynthesis. In Figure 11a, the observed daily $\delta\text{s}\cdot\Delta\text{CO}_2$ values are compared with the simulated values



534 using the *a priori* anthropogenic CO₂ emissions. Here ΔCO_2 represents the total CO₂ enhancement for
535 both observations and simulations. The product $\delta_s \cdot \Delta\text{CO}_2$ can be interpreted as the regional source term.
536 The average values were -1009.0 (and -841.9) ppm·‰ for observations and -1096.7 (and 1000.5) ppm·‰
537 for model results in 2014 (and 2015). The slope of the regression fit was 0.99 (± 0.12) and the intercept
538 was -151.7 (± 130.1) for all data during the two winters. After applying the monthly scaling factors to
539 constrain the anthropogenic CO₂ emissions, the re-calculated results were closer to the 1:1 line with a
540 slightly improved correlation (R increased from 0.47 to 0.50; Figure 11b). Note that the application of the
541 monthly scaling factors only impacts the ΔCO_2 but not δ_s . The uncertainty in δ_s will be discussed next.

542 3.3.2 Comparison between δ_{ms} and δ_s

543 To evaluate the δ_s simulations, we compared observed and simulated δ_s as displayed in Figure 12a for all-
544 day and nighttime conditions. Here, nighttime simulations were selected to minimize the effects of
545 ecosystem photosynthesis and to focus on the anthropogenic CO₂ sources. Two methods were used to
546 calculate δ_s from the observations including the Miller-Tans and Keeling plot methods. Although δ_s
547 differed between these two methods, both displayed similar seasonal variations with higher values ($\delta^{13}\text{C}$
548 enrichment) in summer and lower values in winter. Such seasonal variations were also observed at other
549 urban sites including Beijing, China (Pang et al., 2016), Bern, Switzerland (Sturm et al., 2006), Bangalore
550 city, India (Guha and Ghosh, 2010), Wroclaw, Poland (Górka and Lewicka-szczebak, 2013).

551 If the CO₂ sources/sinks are homogeneously distributed and without monthly variations, the atmospheric
552 CO₂ enhancement components would remain unchanged, and there would be no seasonal changes in δ_s .
553 In reality, variations in atmospheric transport processes interact with regional CO₂ sink/source changes
554 that cause monthly variations in δ_s . The comparison of δ_s between simulations and observations indicated
555 that the model performed well in capturing the mixing and transport of CO₂ from different sources. We
556 can also infer from their difference that the proportions of some CO₂ categories were biased in the *a*
557 *priori* emission map. This can be caused by both the downscaling of EDGAR inventory distribution to
558 0.1° and the magnitude of some emissions categories. Among all anthropogenic sources, the most
559 significant linear relations were found between the simulated anthropogenic δ_s and cement CO₂
560 proportions for these 24 months, with slopes of 0.33‰ for nighttime and 0.35‰ for all-day conditions (R^2
561 = 0.97, $p < 0.001$; Figure 12 b & c). These results strongly support our hypothesis that cement CO₂
562 emissions dominated monthly δ_s variations in the YRD region.

563 3.3.3 Sensitivity of atmospheric $\delta^{13}\text{C}\text{-CO}_2$ and δ_s to cement CO₂ emissions



564 The discrepancy between simulated and observed δ_s highlights that some CO₂ sources were biased in the
565 *a priori* inventories. As discussed above, cement CO₂ emissions had the most distinct $\delta^{13}\text{C-CO}_2$ end-
566 member value of $0\text{‰} \pm 0.30\text{‰}$. Combined with its large emission, it had a strong potential to influence δ_s ,
567 and $\delta^{13}\text{C-CO}_2$. YRD represents the largest cement producing region in the world. Its relative proportion
568 to total national anthropogenic CO₂ emissions is about 5.5% to 6.5% based on IPCC method and 7.3% for
569 EDGAR. These proportions are 50% greater than the global average of 4% (Boden et al., 2016) and much
570 larger than most countries (Andrew, 2018) and other large urbanized areas such as California (2%; Cui et
571 al., 2019).

572 The local activity data reveals that the cement production increased from 3.55×10^8 tons in 2010 to $4.56 \times$
573 10^8 tons in 2014 in the YRD area. Our own calculation of the national clinker-to-cement indicated a
574 decreasing trend from 64% in 2004 to around 56% in 2015. Here, we applied the value of 61.7% for 2010
575 and the average value of 57.0% for 2014 to 2015. We then used the EF for clinker (0.52 ± 0.01 tonne CO₂
576 per tonne clinker; IPCC 2013). Finally, the calculated cement CO₂ emissions were $1.14 (\pm 0.02) \times 10^8$
577 tonne for 2010 and $1.35 (\pm 0.03) \times 10^8$ tonne for 2014, indicating an 18.4% increase over this time period.
578 This result is close to the scaling factor 1.145 for the total anthropogenic CO₂ emissions for the same
579 period.

580 The cement CO₂ emission was 1.45×10^8 tonne for the EDGAR products in 2010. Applying the scaling
581 factor of 1.184, based on our independent method, the EDGAR cement CO₂ emissions was 1.72×10^8
582 tonne for the year of 2014. The 27% difference between the EDGAR inventory and our independent
583 calculations probably resulted from large errors in the clinker-to-cement ratio and regional activity data.
584 Ke et al. (2013) reported a much higher clinker-to-cement ratio of 73% to 70% for China during 2005 and
585 2007 than the ratio of 57% in 2014 to 2015. If we applied a 70% ratio, the EDGAR cement CO₂ emission
586 would change to 1.28×10^8 tonne for 2010.

587 The monthly cement emission proportions varied from 6.21% to 8.98%, while its enhancement proportion
588 was much larger and could reach 16.85%. In other words, favorable atmospheric transport processes
589 amplified the cement CO₂ enhancement proportion at our observational site (Table S2). To quantify the
590 extent to which the cement CO₂ enhancement components can affect δ_s and atmospheric $\delta^{13}\text{C-CO}_2$ we
591 conducted sensitivity tests by changing the cement enhancement proportions to 0.8, 1.2, 1.4, 1.6, 1.8, and
592 2 times its original value. These sensitivity tests are based on two different assumptions for cement CO₂
593 enhancement changes: (1) There is no bias in the total anthropogenic CO₂ enhancement such that a
594 proportional increase/decrease in the cement component does not change the relative anthropogenic
595 contributions; (2) Only the cement enhancement changes. From equation 2, these two assumptions will
596 change both δ_s and $\delta^{13}\text{C-CO}_2$ but with different amplitude.



597 Results for the first assumption are shown in Figure 13a-b for both nighttime and all-day δ_s simulations.
598 The simulated δ_s increased linearly with the increase of cement proportions, at a rate of 2.73‰ increase
599 per 10% increase of cement proportions in the nighttime and 2.72‰ for all-day. The result for the second
600 assumption is relatively similar with the first one, yielding a 2.32‰ increase for a 10% increase in the
601 cement proportion. As shown in Table S2, the cement CO₂ enhancement proportions increased from 5.60%
602 - 6.77% (December) to 13.16% - 16.85% (June), which is the primary cause for the observed monthly δ_s
603 variations. The high sensitivity of δ_s to cement CO₂ proportions can partly explain the relative difference
604 of modeled δ_s and indicates a potential advantage to constrain cement CO₂ emissions by using
605 atmospheric $\delta^{13}\text{C-CO}_2$ observations. Finally we calculated how cement CO₂ can change atmospheric
606 $\delta^{13}\text{C-CO}_2$ (Figure 13c). These results show that atmospheric $\delta^{13}\text{C-CO}_2$ is more sensitive to the first
607 assumption than the second assumption. These sensitivity analyses indicate that a cement CO₂
608 enhancement relative change of 20% (or 1.57% increase) can cause a 0.013‰ - 0.038‰ change in the
609 atmospheric $\delta^{13}\text{C-CO}_2$. These results indicate that δ_s is more sensitive to cement CO₂ emissions compared
610 with other anthropogenic and biological CO₂ sources/sinks.

611 4 Conclusions

- 612 (1) Total annual anthropogenic CO₂ emissions for the YRD showed high consistency between the top-
613 down and bottom-up approaches with a bias less than 6%.
- 614 (2) Approximately 59% and 41% of the $\delta^{13}\text{C-CO}_2$ seasonality were attributed to the change in $\delta^{13}\text{C}$
615 background value and the regional CO₂ source term, respectively.
- 616 (3) Power industry and oil refineries/ transformation industry together contributed 0.40‰, accounting
617 for 64.5% of all regional source terms (0.62‰).
- 618 (4) If excluding all ecosystem respiration and photosynthetic discrimination in YRD area, $\delta^{13}\text{C-CO}_2$
619 seasonality will increase from 1.53‰ to 1.66‰.
- 620 (5) Atmospheric transport processes in summer amplified the cement CO₂ enhancement proportions in
621 the YRD area, which dominated monthly δ_s variations. δ_s was shown to be a strong linear relation
622 with cement CO₂ proportion in the YRD area.

623 Acknowledgements

624 This research was partially supported by start-up foundation (163108094) from Nanjing Forestry
625 University, Natural Science Foundation of Jiangsu Province (BK20181100), and
626 Key Research Foundation of Jiangsu Meteorological Society (KZ201803).

627 Code/Data availability



628 The data presented in this manuscript has been uploaded on our group website:

629 <https://yncenter.sites.yale.edu/data-access>.

630 **Author contribution:** Cheng Hu, Timothy J. Griffis and Xuhui Lee designed the study, Cheng
631 Hu performed the model simulation, Cheng Hu write the original draft, Supervision: Timothy J.
632 Griffis and Xuhui Lee, Data acquisition: Jiaping Xu, Wenjing Huang, Dong Yang, Yan Chen,
633 Cheng Liu, Shoudong Liu, and Lichen Deng, all co-authors contributed to the data analysis.

634 **Competing interests:** The authors declare that they have no conflict of interest.

635

636 **References:**

- 637 Alden, C. B., Miller, J. B., and Gatti, L. V.: Regional atmospheric CO₂ inversion reveals seasonal and geographic
638 differences in Amazon net biome exchange, *Global Change Biology*, 22, 3427–3443,
639 <https://doi.org/10.1111/gcb.13305>, 2016.
- 640 Andrew, R. M.: Global CO₂ emissions from cement production, *Earth System Science Data*, 10, 2213–2239.
641 <https://doi.org/10.5194/essd-2017-77>, 2018.
- 642 Ballantyne, A. P., Miller, J. B., Baker, I. T., Tans, P. P., and White, J. W. C.: Novel applications of carbon isotopes
643 in atmospheric CO₂: what can atmospheric measurements teach us about processes in the biosphere? *Biogeosciences*,
644 8, 3093–3106, <https://doi.org/10.5194/bg-8-3093-2011>, 2011.
- 645 Boden, T., Andres, R., and Marland, G.: Global, Regional, and National Fossil-Fuel CO₂ Emissions (1751 - 2013)
646 (V. 2016) [Data set]. Environmental System Science Data Infrastructure for a Virtual Ecosystem; Carbon Dioxide
647 Information Analysis Center (CDIAC), Oak Ridge National Laboratory (ORNL), Oak Ridge, TN (United States).
- 648 Berezin, E. V., Konovalov, I. B., Ciais, P., Richter, A., Tao, S., Janssens-Maenhout, G., Beekmann, M., and Schulze,
649 E.-D.: Multiannual changes of CO₂ emissions in China: indirect estimates derived from satellite measurements of
650 tropospheric NO₂ columns, *Atmos. Chem. Phys.*, 13, 9415–9438, <https://doi.org/10.5194/acp-13-9415-2013>, 2013.
- 651 Brioude, J., Angevine, W. M., Ahmadov, R., Kim, S.-W., Evan, S., McKeen, S. A., Hsie, E.-Y., Frost, G. J.,
652 Neuman, J. A., Pollack, I. B., Peischl, J., Ryerson, T. B., Holloway, J., Brown, S. S., Nowak, J. B., Roberts, J. M.,
653 Wofsy, S. C., Santoni, G. W., Oda, T., and Trainer, M.: Top-down estimate of surface flux in the Los Angeles Basin
654 using a mesoscale inverse modeling technique: assessing anthropogenic emissions of CO, NO_x and CO₂ and their
655 impacts, *Atmos. Chem. Phys.*, 13, 3661–3677, <https://doi.org/10.5194/acp-13-3661-2013>, 2013.
- 656 Bréon, F. M., Broquet, G., Puygrenier, V., Chevallier, F., Xueref-Remy, I., Ramonet, M., Dieudonné, E., Lopez, M.,
657 Schmidt, M., Perrussel, O., and Ciais, P.: An attempt at estimating Paris area CO₂ emissions from atmospheric
658 concentration measurements, *Atmos. Chem. Phys.*, 15, 1707–1724, <https://doi.org/10.5194/acp-15-1707-2015>, 2015.
- 659 Cao, C., Lee, X., Liu, S., Schultz, N., Xiao, W., Zhang, M., and Zhao, L.: Urban heat islands in China enhanced by
660 haze pollution. *Nature Communications*, 7(1), doi: 10.1038/ncomms12509, 2016.
- 661 Chen, B., Chen J., Tans, P., and Huang L.: Simulating dynamics of δ¹³C of CO₂ in the planetary boundary layer over
662 a boreal forest region: covariation between surface fluxes and atmospheric mixing, *Tellus*, 537–549,
663 <https://doi.org/10.1111/j.1600-0889.2006.00213.x>, 2006.
- 664 Chen, J. M., Mo, G., and Deng, F.: A joint global carbon inversion system using both CO₂ and ¹³CO₂ atmospheric
665 concentration data, *Geosci. Model Dev. Discuss.*, doi:10.5194/gmd-2016-53, 2016.



- 666 Cai B., Wang J., He J., and Geng Y.: Evaluating CO₂ emission performance in China's cement industry: An
667 enterprise perspective. *Applied Energy*, 2015.11.006, <https://doi.org/10.1016/j.apenergy.2015.11.006>, 2015.
- 668 Cui, X., Newman, S., Xu, X., Andrews, A. E., Miller, J., Lehman, S.: Atmospheric observation-based estimation of
669 fossil fuel CO₂ emissions from regions of central and southern California. *Science of the Total Environment*, 664,
670 381–391, <https://doi.org/10.1016/j.scitotenv.2019.01.081>, 2019.
- 671 Deng L., Liu S., and Zhao X., Study on the change in land cover of Yangtze River Delta based on MOD13A2 data,
672 *China Science Paper*, 000(015):1822-1827 (in Chinese).
- 673 Gately, C. K., Hutyra, L. R., and Wing, I. S.: Cities, traffic, and CO₂: A multidecadal assessment of trends, drivers,
674 and scaling relationships, *Proceedings of the National Academy of Sciences of the United States of America*, 112(16),
675 4999–5004, <https://doi.org/10.1073/pnas.1421723112>, 2015.
- 676 Gately, C. K., and Hutyra, L. R.: Large uncertainties in urban-scale carbon emissions. *Journal of Geophysical*
677 *Research: Atmospheres*, 122, 11,242–11,260, <https://doi.org/10.1002/2017JD027359>, 2017.
- 678 Graven, H. D., Fischer, M. L., Lueker, T., Jeong, S., Guilderson, T. P., Keeling, R.: Assessing fossil fuel CO₂
679 emissions in California using atmospheric observations and models. *Environmental Research Letters*, 13(2018)
680 065007, <https://doi.org/10.1088/1748-9326/aabd43>, 2018.
- 681 Griffis, T. J., Sargent, S., Baker, J., Lee, X., Tanner, B., Greene, J., Swiatek, E., and K. Billmark K.: Direct
682 measurement of biosphere-atmosphere isotopic CO₂ exchange using the eddy covariance technique, *Journal of*
683 *Geophysical Research: Atmospheres*, 113, D08304, 2008.
- 684 Griffis, Timothy J.: Agricultural and Forest Meteorology Tracing the flow of carbon dioxide and water vapor
685 between the biosphere and atmosphere: A review of optical isotope techniques and their application. *Agricultural*
686 *and Forest Meteorology*, 174–175, 85–109, 2013.
- 687 Górka, M., and Lewicka-Szczepak, D.: One-year spatial and temporal monitoring of concentration and carbon
688 isotopic composition of atmospheric CO₂ in a Wrocław (SW Poland) city area. *Applied Geochemistry*, 35:7-13,
689 <https://doi.org/10.1016/j.apgeochem.2013.05.010>, 2013.
- 690 Guha, T., and Ghosh, P.: Diurnal variation of atmospheric CO₂ concentration and δ¹³C in an urban atmosphere
691 during winter-role of the Nocturnal Boundary Layer. *Journal of Atmospheric Chemistry*, 65(1), 1–12, <https://doi.org/10.1007/s10874-010-9178-6>, 2010.
- 693 Hu, C., Liu, S., Wang, Y., Zhang, M., Xiao, W., Wang, W., and Xu, J.: Anthropogenic CO₂ emissions from a
694 megacity in the Yangtze River Delta of China. *Environmental Science and Pollution Research*, 25(23), 23157–
695 23169, <https://doi.org/10.1007/s11356-018-2325-3>, 2018.
- 696 Hu, C., Griffis, T. J., Liu, S., Xiao, W., Hu, N., Huang, W., Yang D., and Lee X.: Anthropogenic methane emission
697 and its partitioning for the Yangtze River Delta region of China. *Journal of Geophysical Research: Biogeosciences*,
698 124, <https://doi.org/10.1029/2018JG004850>, 2019.
- 699 Hu, C., Griffis, T. J., Lee, X., Millet, D. B., Chen, Z., Baker, J. M., and Xiao, K.: Top-Down constraints on
700 anthropogenic CO₂ emissions within an agricultural-urban landscape. *Journal of Geophysical Research:*
701 *Atmospheres*, 123(9), 4674–4694, <https://doi.org/10.1029/2017JD027881>, 2018b.
- 702 Hu, L., Andrews, A. E., Thoning, K. W., Sweeney, C., Miller, J. B., Michalak, A. M.: Enhanced North American
703 carbon uptake associated with El Niño. *Science Advances*, 5, eaaw0076, <https://doi.org/10.1126/sciadv.aaw0076>,
704 2019.
- 705 He, J., Naik, V., Horowitz, L. W., Dlugokencky, E., and Thoning, K.: Investigation of the global methane budget
706 over 1980–2017 using GFDL-AM4.1, *Atmos. Chem. Phys.*, 20, 805–827, <https://doi.org/10.5194/acp-20-805-2020>,
707 2020.



- 708 Intergovernmental Panel on Climate Change (IPCC). Climate change: The physical science basis. In T. F. Stocker,
709 D. Qin, G.-K. Plattner, et al. (Eds.), Contribution of Working Group I to the Fifth Assessment Report of the
710 Intergovernmental Panel on Climate Change (Chapter 6, Table 6.1, p. 22). Cambridge, United Kingdom and New
711 York: Cambridge University Press, 2013.
- 712 IEA, 2012. CO₂ Emissions from Fuel Combustion 1971–2010, 2012 Edition. International Energy Agency (IEA),
713 Paris 2012.
- 714 Janssens-Maenhout, G., Crippa, M., Guizzardi, D., Muntean, M., Schaaf, E., Dentener, F.: EDGAR v4.3.2 Global
715 Atlas of the three major Greenhouse Gas Emissions for the period 1970–2012. Earth System Science Data
716 Discussions, (August), 1–55. <https://doi.org/10.5194/essd-2017-79>, 2017.
- 717 Jiang, F., Wang, H. M., Chen, J. M., Machida, T., Zhou, L. X., Ju, W. M., Matsueda, H., and Sawa, Y.: Carbon
718 balance of China constrained by CONTRAIL aircraft CO₂ measurements, *Atmos. Chem. Phys.*, 14, 10133–10144,
719 <https://doi.org/10.5194/acp-14-10133-2014>, 2014.
- 720 Ke J., Mcneil M., Price L., and Zhou N.: Estimation of CO₂ emissions from China's cement production:
721 Methodologies and uncertainties[J]. *Energy Policy*, 57:172-181, <https://doi.org/10.1016/j.enpol.2013.01.028>, 2013.
- 722 Keeling, C. D.: The concentration and isotopic abundances of carbon dioxide in the atmosphere. *Tellus*, 12(2), 200–
723 203. Keeling, C. D. (1961). The concentration and isotopic abundances of carbon dioxide in rural and marine air.
724 *Geochimica et Cosmochimica Acta*, 24(3-4), 277–298, <https://doi.org/10.1111/j.2153-3490.1960.tb01300.x>, 1960.
- 725 Lai, C., Ehleringer, J. R., Tans, P., and Wofsy, S. C.: Estimating photosynthetic ¹³C discrimination in terrestrial CO₂
726 exchange from canopy to regional scales, *Global Biogeochemical Cycles*, 18, GB1041,
727 <https://doi.org/10.1029/2003gb002148>, 2014.
- 728 Li, X., and Xiao, J.: A global, 0.05-degree product of solar-induced chlorophyll fluorescence derived from OCO-2,
729 MODIS, and reanalysis data. *Remote Sensing*, 11, 517, <https://doi.org/10.3390/rs11050517>, 2019.
- 730 Lauvaux, T., Miles, N. L., Deng, A., Richardson, S. J., Cambaliza, M. O., Davis, K. J., and Wu K.: High-resolution
731 atmospheric inversion of urban CO₂ emissions during the dormant season of the Indianapolis flux experiment
732 (INFLUX). *Journal of Geophysical Research: Atmospheres*, 121(10), 5213–5236,
733 <https://doi.org/10.1002/2015JD024473>, 2016.
- 734 Martin, C. R., Zeng, N., Karion, A., Mueller, K., Ghosh, S., Lopez-coto, I.: Investigating sources of variability and
735 error in simulations of carbon dioxide in an urban region. *Atmospheric Environment*, 199, 55–69,
736 <https://doi.org/10.1016/j.atmosenv.2018.11.013>, 2019.
- 737 Moore, J., & Jacobson, A. D. (2015). Seasonally varying contributions to urban CO₂ in the Chicago, Illinois, USA
738 region: Insights from a high-resolution CO₂ concentration and δ¹³C record, *Elementa: Science of the Anthropocene*,
739 3:000052.
- 740 Mueller, K., Yadav, V., Lopez-Coto, I., Karion, A., Gourdji, S., Martin, C., and Whetstone, J.: Siting Background
741 Towers to Characterize Incoming Air for Urban Greenhouse Gas Estimation: A Case Study in the Washington,
742 DC/Baltimore Area. *Journal of Geophysical Research: Atmospheres*, 123(5), 2910–2926,
743 <https://doi.org/10.1002/2017JD027364>, 2018.
- 744 McManus, J.B., Nelson, D.D., Zahniser, M.S.: Long-term continuous sampling of ¹²CO₂, ¹³CO₂ and ¹²C¹⁸O¹⁶O in
745 ambient air with a quantum cascade laser spectrometer. *Isotopes in Environmental and Health Studies*, 46:1, 49-63,
746 <https://doi.org/10.1080/10256011003661326>, 2010.
- 747 Miller, J. B., Tans, P. P., White, J. W. C., Conway, T. J., and Vaughn, B. W.: The atmospheric signal of terrestrial
748 carbon isotopic discrimination and its implication for partitioning carbon fluxes, *Tellus B*, 55, 197–206,
749 <https://doi.org/10.1034/j.1600-0889.2003.00019.x>, 2003.



- 750 Nathan, B., Lauvaux, T., Turnbull, J. C., and Richardson, S.: Source Sector Attribution of CO₂ Emissions Using an
751 Urban CO/CO₂ Bayesian Inversion System. *Journal of Geophysical Research: Atmospheres*, 123, 13611–13621,
752 <https://doi.org/10.1029/2018JD029231>, 2018.
- 753 Newman, S., Xu, X., Affek, H. P., Stolper, E., and Epstein S.: Changes in mixing ratio and isotopic composition of
754 CO₂ in urban air from the Los Angeles basin, California, between 1972 and 2003, *Journal of Geophysical Research*,
755 113, D23304, <https://doi.org/10.1029/2008JD009999>, 2008.
- 756 Newman, S., Xu, X., Gurney, K. R., Hsu, Y. K., Li, K. F., Jiang, X., Keeling, R., Feng, S., O’Keefe, D., Patarasuk,
757 R., Wong, K. W., Rao, P., Fischer, M. L., and Yung, Y. L.: Toward consistency between trends in bottom-up
758 CO₂ emissions and top-down atmospheric measurements in the Los Angeles megacity, *Atmos. Chem. Phys.*, 16,
759 3843–3863, <https://doi.org/10.5194/acp-16-3843-2016>, 2016.
- 760 Oda, T., Maksyutov, S., and Andres, R. J.: The Open-source Data Inventory for Anthropogenic CO₂, version 2016
761 (ODIAC2016): a global monthly fossil fuel CO₂ gridded emissions data product for tracer transport simulations and
762 surface flux inversions, *Earth Syst. Sci. Data*, 10, 87–107, <https://doi.org/10.5194/essd-10-87-2018>, 2018.
- 763 Pang, J., Wen, X., and Sun, X.: Mixing ratio and carbon isotopic composition investigation of atmospheric CO₂ in
764 Beijing, China. *Science of the Total Environment*, 539, 322–330, <https://doi.org/10.1016/j.scitotenv.2015.08.130>,
765 2016.
- 766 Peters, W., Jacobson, A. R., Sweeney, C., Andrews, A. E., Conway, T. J., Masarie, K., John B. M., Lori M.
767 P. B., Gabrielle P., Adam I. H., Douglas E. J. W., Guido R. v., James T. R., Paul O. W., Maarten C. K., and Pieter P.
768 T.: An atmospheric perspective on North American carbon dioxide exchange: CarbonTracker. *Proceedings of the*
769 *National Academy of Sciences*, 104(48), 18925–18930, <https://doi.org/10.1073/pnas.0708986104>, 2007.
- 770 Pataki, D. E., Bowling, D. R., Ehleringer, J. R., and Zobitz, J. M.: High resolution atmospheric monitoring of urban
771 carbon dioxide sources, *Geophysical Research Letter*, 33, L03813, <https://doi.org/10.1029/2005GL024822>, 2006.
- 772 Pillai, D., Buchwitz, M., Gerbig, C., Koch, T., Reuter, M., Bovensmann, H., Marshall, J., and Burrows, J. P.:
773 Tracking city CO₂ emissions from space using a high-resolution inverse modelling approach: a case study for Berlin,
774 Germany, *Atmos. Chem. Phys.*, 16, 9591–9610, <https://doi.org/10.5194/acp-16-9591-2016>, 2016.
- 775 Ruckstuhl, A. F., Henne, S., Reimann, S., Steinbacher, M., Vollmer, M. K., O’Doherty, S., Buchmann, B., and
776 Hueglin, C.: Robust extraction of baseline signal of atmospheric trace species using local regression, *Atmos. Meas.*
777 *Tech.*, 5, 2613–2624, <https://doi.org/10.5194/amt-5-2613-2012>, 2012.
- 778 State Statistical Bureau. China Statistical Yearbook 2015; China Statistical Press: Beijing, China, 2016. (In Chinese)
- 779 Seto, K. C., Dhakal, S., Bigio, A., Blanco, H., Delgado, G. C., and Dewar, D.: Human settlements, infrastructure,
780 and spatial planning. In O. Edenhofer, et al. (Eds.), *Climate change 2014: Mitigation of climate change. Contribution*
781 *of working group III to the fifth assessment report of the intergovernmental panel on climate change* (pp. 923–1000).
782 Cambridge, UK and New York, NY, USA: Cambridge University Press.
783 <https://doi.org/10.1017/CBO9781107415416.018>, 2014.
- 784 Thoning, K. W., Tans, P. P., and Komhyr, W. D.: Atmospheric carbon dioxide at Mauna Loa observatory 2.
785 Analysis of the NOAA/GMCC data, 1974–1985. *Journal of Geophysical Research: Atmospheres*, 94(D6), 8549–
786 8565, <https://doi.org/10.1029/JD094iD06p08549>, 1989.
- 787 Wang, Y., Munger, J. W., Xu, S., McElroy, M. B., Hao, J., Nielsen, C. P., and Ma, H.: CO₂ and its correlation with
788 CO at a rural site near Beijing: implications for combustion efficiency in China, *Atmos. Chem. Phys.*, 10, 8881–
789 8897, <https://doi.org/10.5194/acp-10-8881-2010>, 2010.
- 790 Zhang, H. F., Chen, B. Z., van der Laan-Luijkx, I. T., Chen, J., Xu, G., Yan, J. W., Zhou, L. X., Fukuyama, Y., Tans,
791 P. P., and Peters W.: Net terrestrial CO₂ exchange over China during 2001–2010 estimated with an ensemble data



- 792 assimilation system for atmospheric CO₂, *Journal of Geophysical Research: Atmospheres*, 119, 3500–3515,
793 <https://doi.org/10.1002/2013JD021297>, 2014.
- 794 Rayner, P. J., Raupach, M. R., Paget, M., Peylin, P., and Koffi, E.: A new global gridded data set of CO₂ emissions
795 from fossil fuel combustion : Methodology and evaluation, *Journal of Geophysical Research: Atmospheres*. 115,
796 D19306, <https://doi.org/10.1029/2009JD013439>, 2010.
- 797 Ribeiro, H. V., Rybski, D., and Kropp, J. P.: Effects of changing population or density on urban carbon dioxide
798 emissions. *Nature Communications*, (2019), 1–9, <https://doi.org/10.1038/s41467-019-11184-y>, 2019.
- 799 Sargent, M., Barrera, Y., Nehrkorn, T., Hutyra, L. R., Gately, C. K., Mckain, K., Sweeney, C., Hegarty, J.,
800 Hardiman, B., Steven C. Wofsy, S. C.: Anthropogenic and biogenic CO₂ fluxes in the Boston urban region,
801 *Proceedings of the National Academy of Sciences of the United States of America*. 115(40),
802 <https://doi.org/10.1073/pnas.1803715115>, 2018.
- 803 Schneising, O., Heymann, J., Buchwitz, M., Reuter, M., Bovensmann, H., and Burrows, J. P.: Anthropogenic carbon
804 dioxide source areas observed from space: assessment of regional enhancements and trends, *Atmos. Chem. Phys.*,
805 13, 2445–2454, <https://doi.org/10.5194/acp-13-2445-2013>, 2013.
- 806 Stauffer, J., Broquet, G., Bréon, F.-M., Puygrenier, V., Chevallier, F., Xueref-Rémy, I., Dieudonné, E., Lopez, M.,
807 Schmidt, M., Ramonet, M., Perrussel, O., Lac, C., Wu, L., and Ciais, P.: The first 1-year-long estimate of the Paris
808 region fossil fuel CO₂ emissions based on atmospheric inversion, *Atmos. Chem. Phys.*, 16, 14703–14726,
809 <https://doi.org/10.5194/acp-16-14703-2016>, 2016.
- 810 Sturm, P., Leuenberger, M., Valentino, F. L., Lehmann, B., and Ihly, B.: Measurements of CO₂, its stable isotopes,
811 O₂/N₂, and ²²²Rn at Bern, Switzerland, *Atmos. Chem. Phys.*, 6, 1991–2004, <https://doi.org/10.5194/acp-6-1991-2006>,
812 2006.
- 813 Sturm, P., Tuzson, B., Henne, S., and Emmenegger, L.: Tracking isotopic signatures of CO₂ at the high altitude site
814 Jungfraujoch with laser spectroscopy: analytical improvements and representative results, *Atmos. Meas. Tech.*, 6,
815 1659–1671, <https://doi.org/10.5194/amt-6-1659-2013>, 2013.
- 816 Super, I., Denier van der Gon, H. A. C., van der Molen, M. K., Sterk, H. A. M., Hensen, A., and Peters, W.: A
817 multi-model approach to monitor emissions of CO₂ and CO from an urban–industrial complex, *Atmos. Chem. Phys.*,
818 17, 13297–13316, <https://doi.org/10.5194/acp-17-13297-2017>, 2017.
- 819 Thompson, R. L., Patra, P. K., Chevallier, F., Maksyutov, S., Law, R. M., Ziehn, T., and Ciais P.: Top-down
820 assessment of the Asian carbon budget since the mid 1990s. *Nature Communications*, 7, 1–10,
821 <https://doi.org/10.1038/ncomms10724>, 2016.
- 822 Turnbull, J. C., Sweeney, C., Karion, A., Newberger, T., Lehman, S. J., Tans P. P., Davis, K.: Toward
823 quantification and source sector identification of fossil fuel CO₂ emissions from an urban area: results from the
824 influx experiment. *Journal of Geophysical Research: Atmospheres*, 120(1, 292):–312,
825 <https://doi.org/10.1002/2014JD022555>, 2015.
- 826 Turner, A. J., Shusterman, A. A., McDonald, B. C., Teige, V., Harley, R. A., and Cohen, R. C.: Network design for
827 quantifying urban CO₂ emissions: assessing trade-offs between precision and network density, *Atmos. Chem. Phys.*,
828 16, 13465–13475, <https://doi.org/10.5194/acp-16-13465-2016>, 2016.
- 829 Vardag, S. N., Gerbig, C., Janssens-Maenhout, G., and Levin, I.: Estimation of continuous anthropogenic CO₂:
830 model-based evaluation of CO₂, CO, δ¹³C(CO₂) and Δ¹⁴C(CO₂) tracer methods, *Atmos. Chem. Phys.*, 15, 12705–
831 12729, <https://doi.org/10.5194/acp-15-12705-2015>, 2015.
- 832 Verhulst, K. R., Karion, A., Kim, J., Salameh, P. K., Keeling, R. F., Newman, S., Miller, J., Sloop, C., Pongetti, T.,
833 Rao, P., Wong, C., Hopkins, F. M., Yadav, V., Weiss, R. F., Duren, R. M., and Miller, C. E.: Carbon dioxide and



- 834 methane measurements from the Los Angeles Megacity Carbon Project – Part 1: calibration, urban enhancements,
835 and uncertainty estimates, *Atmos. Chem. Phys.*, 17, 8313–8341, <https://doi.org/10.5194/acp-17-8313-2017>, 2017.
- 836 Worden, H. M., Cheng, Y., Pfister, G., Carmichael, G. R., Zhang, Q., Streets, D. G.: Satellite-based estimates of
837 reduced CO and CO₂ emissions due to traffic restrictions during the 2008 Beijing Olympics, *Geophysical Research*
838 *Letters*, 39, 1–6, <https://doi.org/10.1029/2012GL052395>, 2012.
- 839 Xu, J., Lee, X., Xiao, W., Cao, C., Liu, S., Wen, X., Xu, J., Zhang, Z., and Zhao, J.: Interpreting the ¹³C/¹²C ratio of
840 carbon dioxide in an urban airshed in the Yangtze River Delta, China, *Atmos. Chem. Phys.*, 17, 3385–3399,
841 <https://doi.org/10.5194/acp-17-3385-2017>, 2017.
- 842 Yang, Y., Wang, L., Cao, Z. Mou C., Shen, L., Zhao, J., and Fang, Y.: CO₂ emissions from cement industry in China:
843 A bottom-up estimation from factory to regional and national levels. *Journal of Geographical Science*, 27, 711–730.
- 844 Zhao, C., Andrews, A. E., Bianco, L., Eluszkiewicz, J. Hirsh, A., Macdonald, C., Nehr Korn, T., and Fischer M. L.,.
845 Atmospheric inverse estimates of methane emissions from Central California[J]. *Journal of Geophysical Research:*
846 *Atmospheres*, 2009, 114(D16): 4723-4734, <https://doi.org/10.1029/2008JD011671>, 2009.
- 847
- 848
- 849
- 850
- 851
- 852
- 853
- 854
- 855
- 856
- 857
- 858
- 859
- 860
- 861
- 862
- 863



864 **Figure 1.** (a) Weather Research and Forecasting Model simulation domains and the location of WLG site, (b) cement production
865 distribution in YRD and Eastern China.

866 **Figure 2.** (a) Annual anthropogenic CO₂ emissions for study domain (units: nmol m⁻² s⁻¹) and population density in 4 megacities
867 (units: people per hectare) including Nanjing, Hefei, Zhejiang, and Shanghai for the year of 2015, (b) Two-year average
868 concentration footprint.

869 **Figure 3.** (a) Comparisons of hourly CO₂ mixing ratios between observations and model simulation from September 2013 to
870 August 2015, and monthly averages for (b) whole day, (c) nighttime (22:00-06:00, local time) and (d) daytime (10:00 - 16:00);
871 Model results (red), observations (black), and background (grey).

872 **Figure 4.** (a) Relation between monthly PBL height and change in CO₂ mixing ratio; Time series (2013 to 2015) of (b) NDVI, (c)
873 SIF, and (d) GPP.

874 **Figure 5.** (a) Comparisons of simulated and observed CO₂ enhancement, (b) Simulated anthropogenic CO₂ enhancement
875 proportion for the main sources, and (c) CO₂ enhancement contributions from different provinces.

876 **Figure 6.** Comparisons among three strategies for calculating the background $\delta^{13}\text{C-CO}_2$. Strategy 1 (WLG discrete: weekly
877 discrete observations at WLG site, WLG CCGCRV: derived hourly data with WLG observations and CCGCRV method);
878 Strategy 2 (Calculated: by choosing clean air in winter); and strategy 3 (M-T method: derived results with observations and M-T
879 approach, M-T CCGCRV: derived hourly results with M-T approach and CCGCRV method, see details in section 2.2.1).

880 **Figure 7.** (a) Comparisons of observed and modeled hourly $\delta^{13}\text{C-CO}_2$ from September 2013 to August 2015, and (b) Simulated
881 hourly biological CO₂ enhancement.

882 **Figure 8.** Comparisons of observed and modeled (a) CO₂ mixing ratio and (b) $\delta^{13}\text{C-CO}_2$ from December 2013 to February 2014;
883 (c) CO₂ mixing ratio and (b) $\delta^{13}\text{C-CO}_2$ from December 2014 to February 2015; (e) CO₂ mixing ratio and (f) $\delta^{13}\text{C-CO}_2$ from
884 June 2014 to August 2014; (g) CO₂ mixing ratio and (h) $\delta^{13}\text{C-CO}_2$ from June 2015 to August 2015.

885 **Figure 9.** Scatter plots of observed versus modeled (a) winter time CO₂ mixing ratios, (b) winter time $\delta^{13}\text{C-CO}_2$, (c) summer
886 time CO₂, and (d) summer time $\delta^{13}\text{C-CO}_2$ for both years.

887 **Figure 10.** Digital filtering curve fitting (CCGCRV) for background, observations, normal simulations, case 1 (excluding
888 photosynthesis), and case 2 (excluding respiration and photosynthesis) in both years, (b) $\delta^{13}\text{C-CO}_2$ comparisons between normal
889 simulations and case 1, and (c) $\delta^{13}\text{C-CO}_2$ comparisons between normal simulations and case 2.

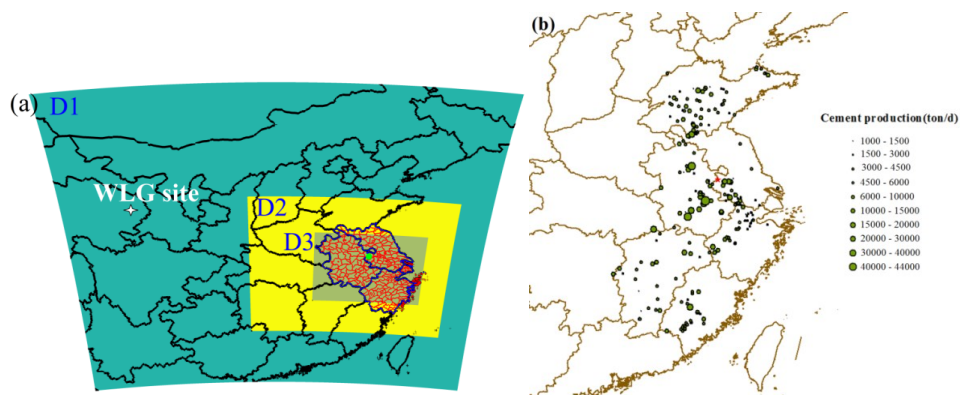
890 **Figure 11.** Comparisons of winter time $\delta\text{s-}\Delta\text{CO}_2$ using (a) *a priori* and (b) constrained anthropogenic CO₂ emissions.

891 **Figure 12.** (a) Comparisons between observed and modeled δs , (b) relationship between cement CO₂ enhancement proportion
892 and simulated anthropogenic δs for nighttime and (c) all-day.

893 **Figure 13.** Sensitivity tests showing the influence of cement CO₂ emissions on δs for (a) nighttime, (b) all-day, and (c) the
894 relation between cement CO₂ and $\delta^{13}\text{C}$ for simulation strategies 1 and 2. Note that the numbers in brackets indicate changes in
895 $\delta^{13}\text{C}$ with cement CO₂ proportion increase by 0.2 times. The x-axis values indicate changing cement enhancement proportions to
896 0.8 1.2, 1.4, 1.6, 1.8, and 2 times the original values.

897

898



899

900

901 Figure 1. (a) Weather Research and Forecasting Model simulation domains and the location of WLG site, (b) cement production

902 distribution in YRD and Eastern China.

903

904

905

906

907

908

909

910

911

912

913

914

915

916

917

918

919

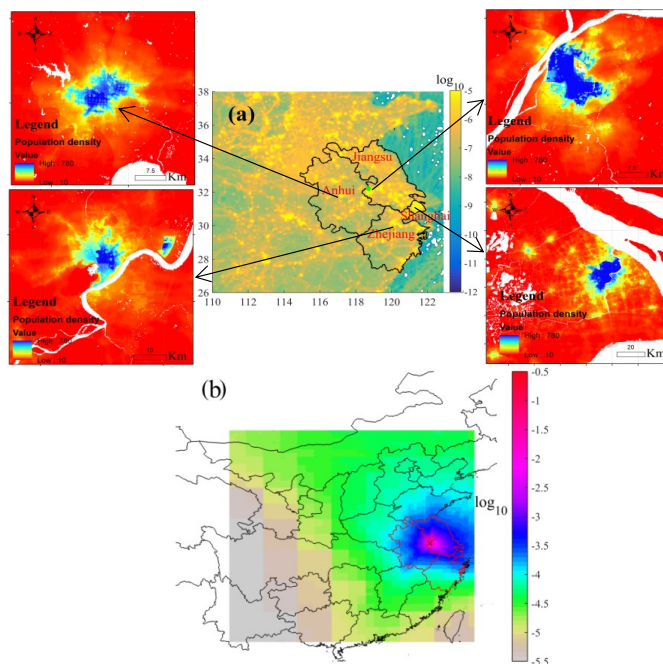
920

921

922



923
924
925
926
927
928
929



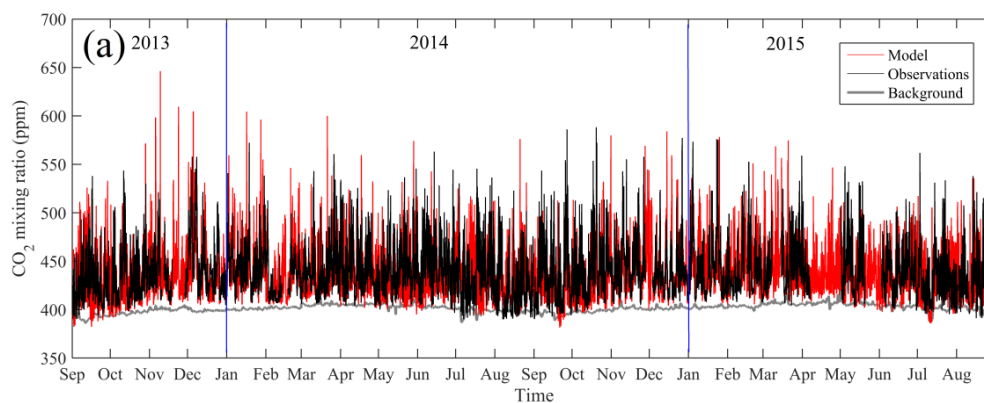
930

931 Figure 2. (a) Annual anthropogenic CO₂ emissions for study domain (units: nmol m⁻² s⁻¹) and population density in 4 megacities
932 (units: people per hectare) including Nanjing, Hefei, Zhejiang, and Shanghai for the year of 2015, (b) Two-year average
933 concentration footprint.

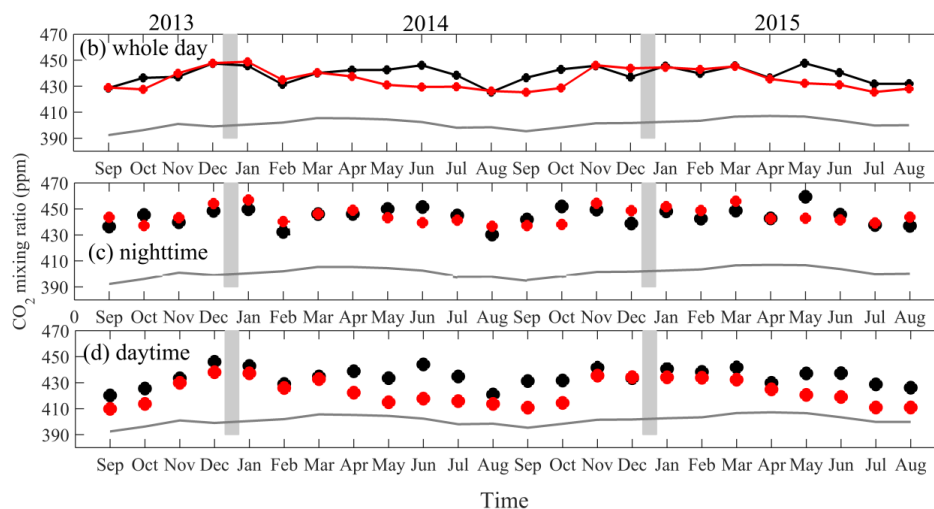
934
935
936
937
938
939
940
941
942
943
944
945
946
947
948



949



950

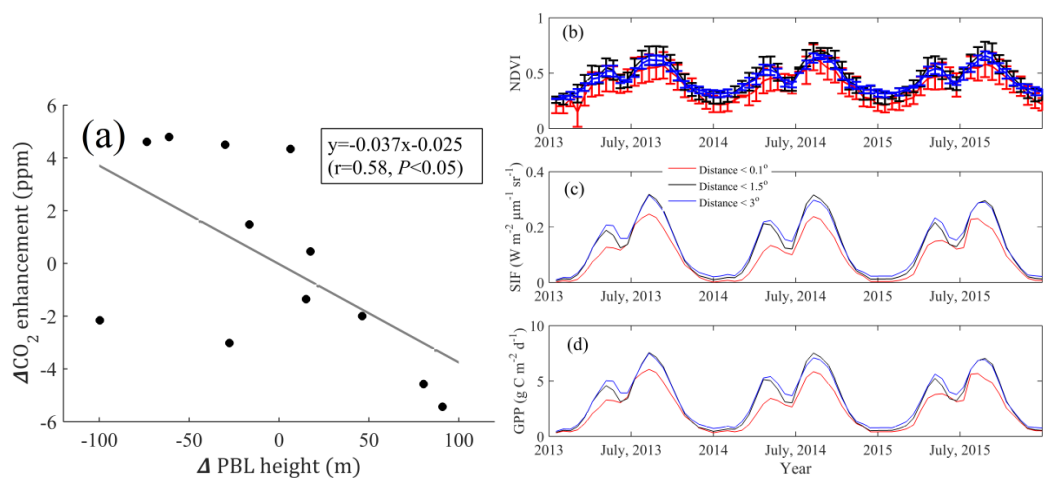


951

952 Figure 3. (a) Comparisons of hourly CO₂ mixing ratios between observations and model simulation from September 2013 to
953 August 2015, and monthly averages for (b) whole day, (c) nighttime (22:00-06:00, local time) and (d) daytime (10:00 - 16:00);
954 Model results (red), observations (black), and background (grey).

955

956



957

958

959 Figure 4. (a) Relation between monthly PBL height and change in CO₂ mixing ratio; Time series (2013 to 2015) of (b) NDVI, (c)
960 SIF, and (d) GPP.

961

962

963

964

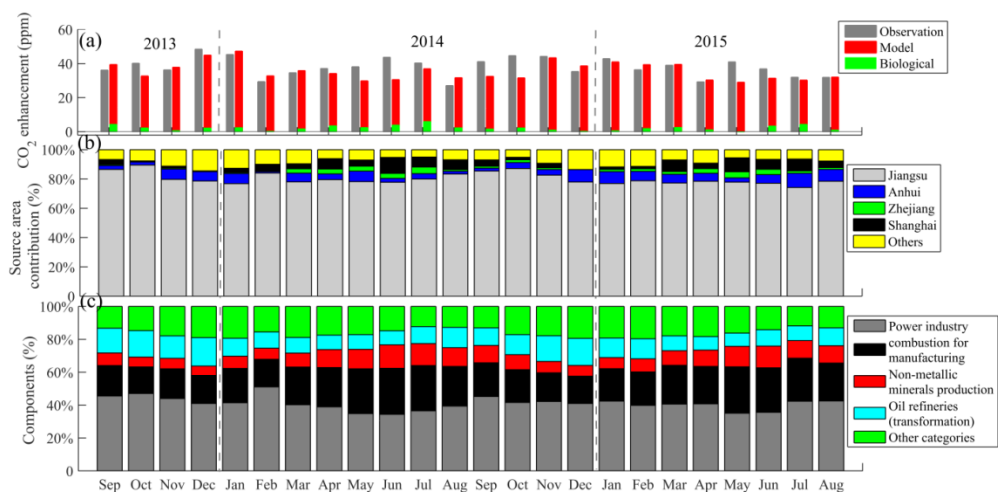
965

966

967

968

969



970

971

972

Figure 5. (a) Comparisons of simulated and observed CO₂ enhancement, (b) Simulated anthropogenic CO₂ enhancement proportion for the main sources, and (c) CO₂ enhancement contributions from different provinces.

973

974

975

976

977

978

979

980

981

982

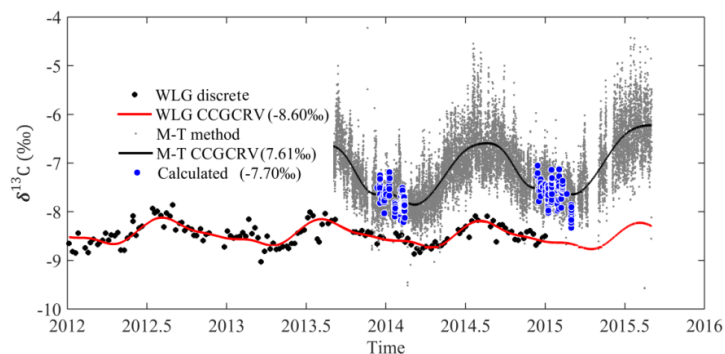
983

984

985

986

987



988

989 Figure 6. Comparisons among three strategies for calculating the background $\delta^{13}\text{C}\text{-CO}_2$. Strategy 1 (WLG discrete: weekly
990 discrete observations at WLG site, WLG CCGCRV: derived hourly data with WLG observations and CCGCRV method);
991 Strategy 2 (Calculated: by choosing clean air in winter); and strategy 3 (M-T method: derived results with observations and M-T
992 approach, M-T CCGCRV: derived hourly results with M-T approach and CCGCRV method, see details in section 2.2.1).

993

994

995

996

997

998

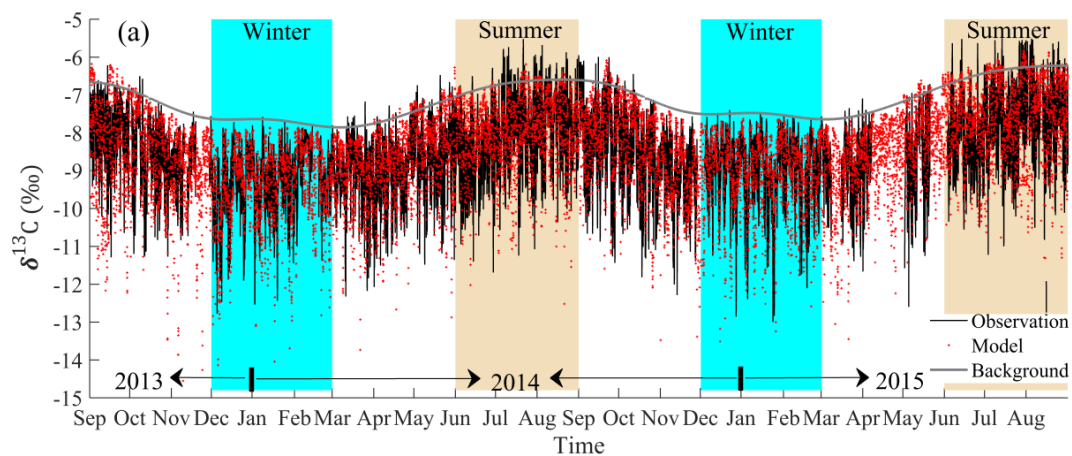
999

1000

1001

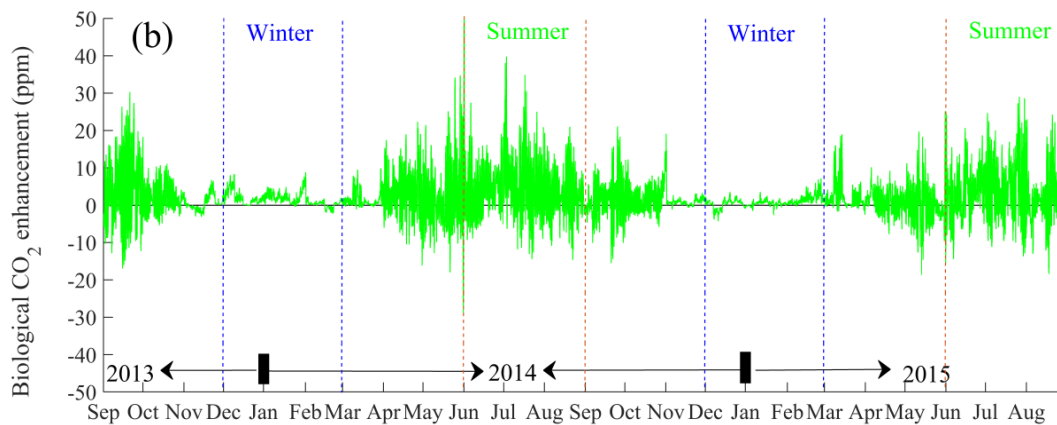
1002

1003



1004

1005

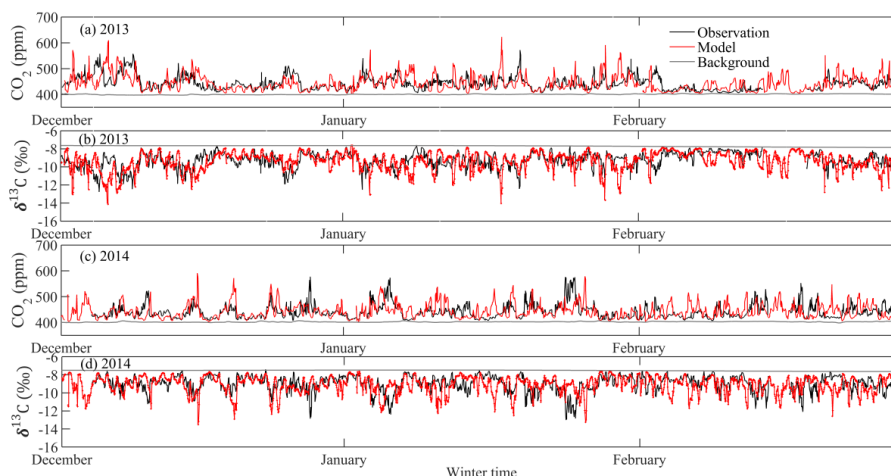


1006

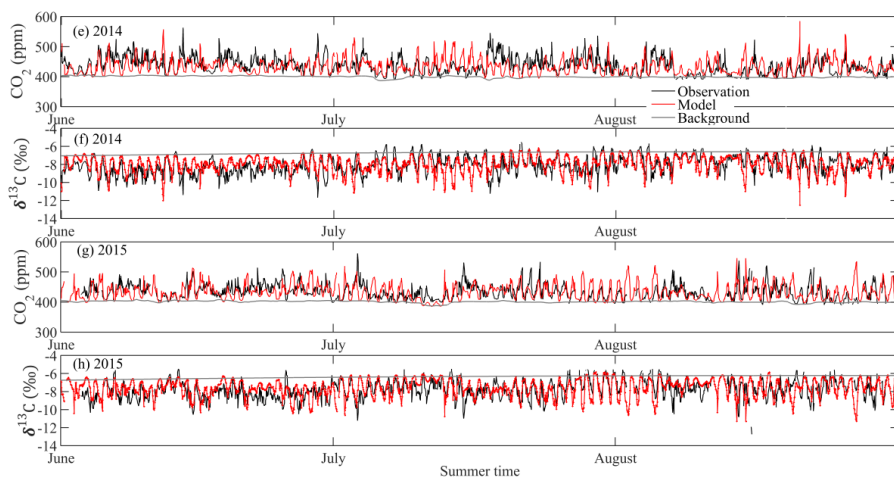
1007 Figure 7. (a) Comparisons of observed and modeled hourly $\delta^{13}\text{C}\text{-CO}_2$ from September 2013 to August 2015, and (b) Simulated
1008 hourly biological CO_2 enhancement.

1009

1010



1011



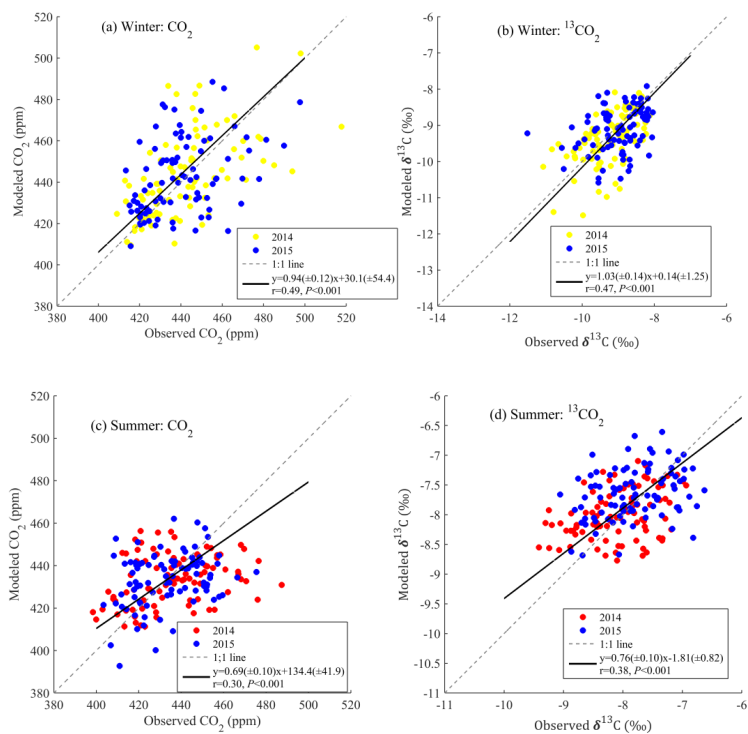
1012

1013 Figure 8. Comparisons of observed and modeled (a) CO₂ mixing ratio and (b) $\delta^{13}\text{C}\text{-CO}_2$ from December 2013 to February 2014;

1014 (c) CO₂ mixing ratio and (b) $\delta^{13}\text{C}\text{-CO}_2$ from December 2014 to February 2015; (e) CO₂ mixing ratio and (f) $\delta^{13}\text{C}\text{-CO}_2$ from

1015 June 2014 to August 2014; (g) CO₂ mixing ratio and (h) $\delta^{13}\text{C}\text{-CO}_2$ from June 2015 to August 2015.

1016



1017

1018

1019 Figure 9. Scatter plots of observed versus modeled (a) winter time CO₂ mixing ratios, (b) winter time $\delta^{13}\text{C}$ -CO₂, (c) summer time
1020 CO₂, and (d) summer time $\delta^{13}\text{C}$ -CO₂ for both years.

1021

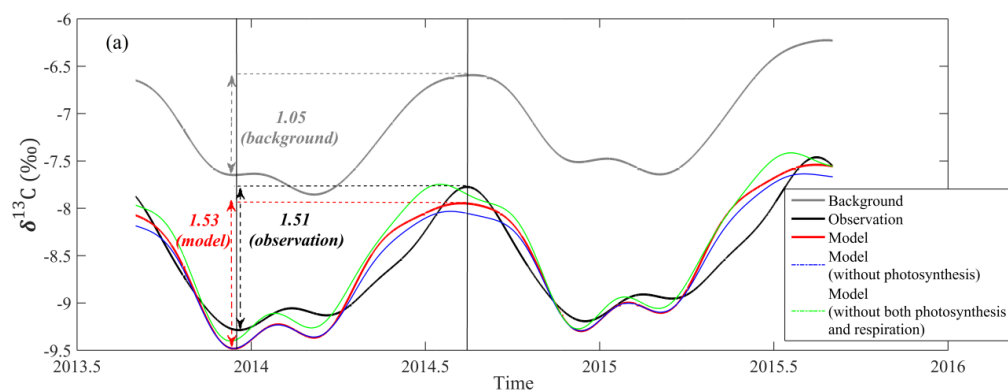
1022

1023

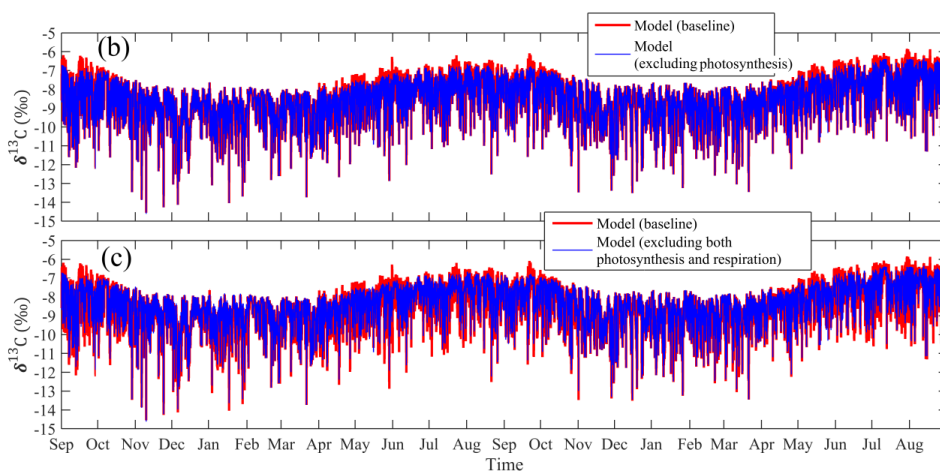
1024

1025

1026



1027

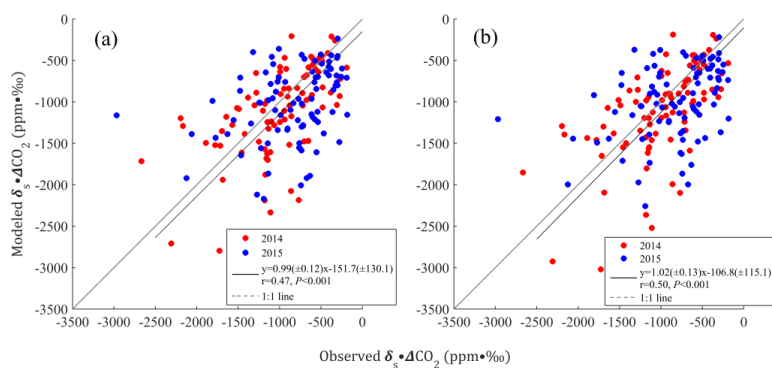


1028

1029 Figure 10. Digital filtering curve fitting (CCGCRV) for background, observations, normal simulations, case 1 (excluding
1030 photosynthesis), and case 2 (excluding respiration and photosynthesis) in both years, (b) $\delta^{13}\text{C}$ -CO₂ comparisons between normal
1031 simulations and case 1, and (c) $\delta^{13}\text{C}$ -CO₂ comparisons between normal simulations and case 2.

1032

1033



1034

1035 Figure 11. Comparisons of winter time $\delta_s \cdot \Delta \text{CO}_2$ using (a) *a priori* and (b) constrained anthropogenic CO_2 emissions.

1036

1037

1038

1039

1040

1041

1042

1043

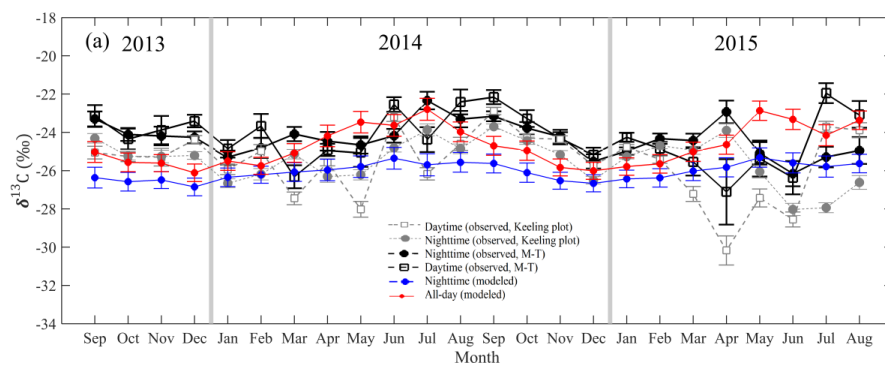
1044

1045

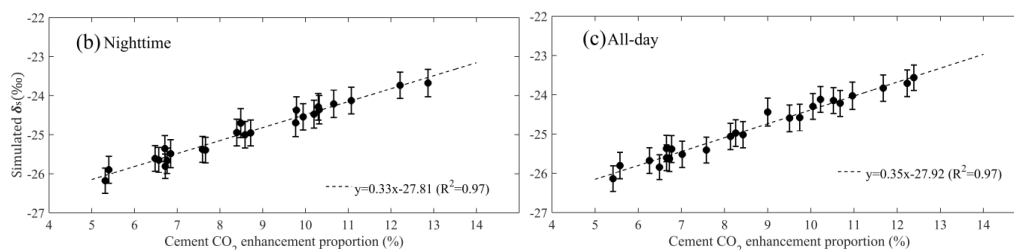
1046

1047

1048



1049



1050

1051 Figure 12. (a) Comparisons between observed and modeled δ_s , (b) relationship between cement CO₂ enhancement proportion and
1052 simulated anthropogenic δ_s for nighttime and (c) all-day.

1053

1054

1055

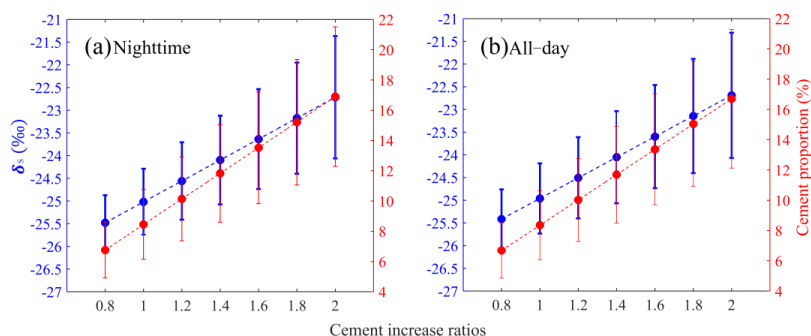
1056

1057

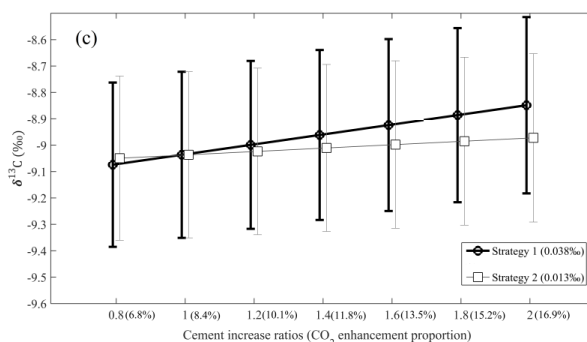
1058

1059

1060



1061



1062

1063

1064

1065

1066

Figure 13. Sensitivity tests showing the influence of cement CO_2 emissions on δ_s for (a) nighttime, (b) all-day, and (c) the relation between cement CO_2 and $\delta^{13}\text{C}$ for simulation strategies 1 and 2. Note that the numbers in brackets indicate changes in $\delta^{13}\text{C}$ with cement CO_2 proportion increase by 0.2 times. The x-axis values indicate changing cement enhancement proportions to 0.8, 1.2, 1.4, 1.6, 1.8, and 2 times the original values.

1067

1068

1069

1070

1071

1072

1073

1074

1075

1076

1077

1078

1079



1080

Table 1. Comparisons of cement and all anthropogenic CO₂ emissions among different methods.

Units: $\times 10^{11}$ kg	Year	EDGAR v432	Inversion results	IPCC method
Cement CO ₂ emissions	2010	1.45	/	1.14
	2014-2015	1.72	/	1.35
All anthropogenic CO ₂ emissions	2010	20.55	/	17.56
	2014-2015	23.53	24.59 ± 2.39	24.38

1081

1082

1083

1084

1085

1086

1087

1088

1089

1090

1091

1092

1093

1094

1095

1096

1097

1098

1099



1100 **Table 2.** Statistical metrics between observed and modeled CO₂ mixing ratios and $\delta^{13}\text{C-CO}_2$ during winter, summer and annual
1101 for 2014 and 2015. Correlation coefficient (R), mean bias (MB), and root mean square error (RMSE) are displayed.

	Years	2014			2015		
		Annual	Winter	Summer	Annual	Winter	Summer
$\delta^{13}\text{C-CO}_2$	R	0.54	0.40	0.47	0.52	0.27	0.39
	RMSE (‰)	1.07	0.94	0.94	1.10	0.92	0.98
	simulation (‰)	-8.68	-9.37	-8.02	-8.45	-9.10	-7.66
	observation (‰)	-8.69	-9.27	-8.09	-8.52	-8.98	-7.83
CO ₂	R	0.38	0.41	0.34	0.35	0.28	0.31
	RMSE (ppm)	29.44	27.48	25.55	30.22	26.81	24.29
	MB (ppm)	2.16	-0.27	3.80	2.99	-0.43	1.53

1102

1103